

Development of Plasmonically Cloaked Nanoparticles

Fuel Cycle

Dr. Eric Burgett

Idaho State University

In collaboration with:

Georgia Institute of Technology

University of Maryland

Daniel Vega, Federal POC

Keith Jewell, Technical POC



Idaho State University

921 South 8th Ave. Stop 8060
Pocatello, ID, 83209-8060
Phone: 2028-282-2220
Email: burgeric@isu.edu

Development of Plasmonically Cloaked Nanoparticles

Final Report

[Intentional Blank Page]

Approved By:

Dr. Eric Burgett, Idaho State University

Dr. Christopher Summers, Georgia Institute of Technology

Dr. Mohamad Al-Sheikhly, University of Maryland

[Intentional Blank Page]

Table of Contents

TABLE OF FIGURES	7
INTRODUCTION	9
PROPOSED SCOPE DESCRIPTION	9
PLASMONIC CLOAK THEORY	9
NEUTRON DETECTION USING METAMATERIALS	10
FLUIDIZED BED REACTOR DESIGN	13
DESIGN OF LARGE AREA ARRAY	14
CURRENT STATUS :	14
DELIVERABLE #1 DOCUMENT REPORTING THE RESPONSE OF THE FIRST PLANAR DEVICES AND INITIAL GROWTH QUALITY OF NEW DETECTOR SYSTEM PROVIDED TO DOE.	14
DELIVERABLE #2 DOCUMENT REPORTING THE RESPONSE OF THE FIRST BAND GAP ENGINEERED SAMPLE DEVICES AND INITIAL GROWTH QUALITY OF NEW DETECTOR SYSTEM PROVIDED TO DOE.	14
DELIVERABLE #3 DOCUMENT REPORTING FIRST NEUTRON SENSOR PERFORMANCE.	19
DELIVERABLE #4 DOCUMENT REPORTING THE OPTIMIZED RESPONSE OF THE FIRST PLANAR NEUTRON DEVICES AND INITIAL GROWTH QUALITY OF NEW DETECTOR SYSTEM PROVIDED TO DOE	19
DELIVERABLE #5 DOCUMENT REPORTING THE COMMISSIONING OF THE REACTOR DATA FOR THE FIRST CLOAKED DEVICES	19
DELIVERABLE #6 BEGIN TO DEVELOP FIRST CLOAKED DEVICES	19
DELIVERABLE #7 DOCUMENT REPORTING THE FIRST CLOAKED NANOPARTICLE BASED RADIATION TESTS DEVELOPED	28
DELIVERABLE #8 DOCUMENT REPORTING THE DESIGN AND POTENTIAL PERFORMANCE OF PROTON RECOIL VERSIONS OF CLOAKED NANOPARTICLES DEVELOPED.	28
DELIVERABLE #9 FINAL REPORT.	28
DELIVERABLE #10 QUARTERLY REPORTS.	28
PLANS FOR NEXT QUARTER	29

BUDGET DATA	29
APPENDIX A – MPB CONTROL FILE FOR PHOTONIC SLAB SCINTILLATOR	30
APPENDIX B – IMAGES OF CURRENT CLOAKING MODEL (MEEP)	33
APPENDIX C – NANOPARTICLE SIZE DATA	35
APPENDIX D – X-RAY DIFFRACTION DATA	36
APPENDIX E – TEM MEASUREMENTS ON NANOPARTICLES - IMAGES	39

Table of Figures

Figure 1 - Nature of Cloak	10
Figure 2 - Design of neutron versus gamma discrimination for design one	11
Figure 3 - Design of neutron versus gamma discrimination for design two	11
Figure 4 - Design of neutron versus gamma discrimination for design three	12
Figure 5 - Design of neutron versus gamma discrimination for design three (no kernel).....	12
Figure 6 - Pulse height distribution from lithium doped ZnO scintillator	13
Figure 7 - Proposed fluidized bed ALD reactor schematic	13
Figure 8 - TM-mode: 13.34% Band Gap	16
Figure 9 - TM-mode: 6.71% Band Gap	16
Figure 10 - TM-mode: 12.53% Band Gap	17
Figure 11 -TM-mode: 13.34% band gap	18
Figure 12 - TM-mode: 13.34% Band Gap	18
Figure 13 - Preliminary SEM images of: A) Al_2O_3 and B) BN.....	20
Figure 14 - TEM Measurement images of: A) $BaTiO_3$ B) Al_2O_3	21
Figure 15 - Fine structure grown from single nucleation site on sapphire. 20mm concentration.	23
Figure 16 - hexagonal rod growth on the surface of sapphire. 50mm concentration.	23
Figure 17 - Planar zinc oxide growth on top of fine structures. 20 mm concentration	24
Figure 19 - Vertically Aligned Hexagonal Rod Growth On The Surface Of Substrate. 100mm Experimental Concentration	25
Figure 20 - Cross section analysis of a 24 hour growth cycle at 90 degree Celsius with a concentration of 30 mm.....	26
Figure 21 - Cross section of 24 hour growth cycle at 90 degrees Celsius with 100 mM experimental concentration. Shows clear depth of multiple micrometers of grown zinc oxide on the surface of the substrate	27
Figure 22 - Preliminary images of cloak model: A) Waveguide controlling the light source B) MEEP output with waveguide marked for reference.....	33
Figure 23 - Additional MEEP images: A) Smaller waveguide to reduce interference B) MEEP output with waveguide marked for reference	33
Figure 24 - Image of model geometry	34

Figure 25 - Nano particle summary of sizes	35
Figure 26 - TEM measurements – sample 2H 001 AL2O3.tif	399
Figure 27 - TEM measurements – sample 2H 003 AL2O3.tif	40
Figure 28 - TEM measurements – sample 2J 002 CeO2.tif.....	41
Figure 29 - TEM measurements – sample 2J 003 CeO2.tif.....	42
Figure 30 - TEM measurements – sample 3C 001 ZrO2.TIF	43
Figure 31 - TEM measurements – sample 3C 003 ZrO2.TIF	44
Figure 32 - TEM measurements – sample 2B 001 WO3.TIF.....	45
Figure 33 - TEM measurements – sample 2B 002 WO3.TIF.....	46
Figure 34 - TEM measurements – sample 1E 001 BaTiO3.TIF.....	47
Figure 35 - TEM measurements – sample 1G 002 BaTiO3.TIF	48
Figure 36 - TEM measurements – sample 4f 001 SiC.TIF.....	49
Figure 37 - TEM measurements – sample 4F 003 SiC.tif	50
Figure 38 - TEM measurements – sample 6F 001 MgO.tif.....	51
Figure 39 - TEM measurements – sample 6F 006 MgO.tif.....	52
Figure 40 - TEM measurements – sample 6J 001 ZnO.tif	53
Figure 41 - TEM measurements – sample 6J 006 ZnO.tif	54
Figure 42 - TEM measurements – sample 7C 002 TiO2.tif	55
Figure 43 - TEM measurements – sample 7C 004 TiO2.tif	56

Introduction

An advanced in-pile multi-parameter reactor monitoring system is being proposed in this funding opportunity. The proposed effort brings cutting edge, high fidelity optical measurement systems into the reactor environment in an unprecedented fashion, including in-core, in-cladding and in-fuel pellet itself. Unlike instrumented leads, the proposed system provides a unique solution to a multi-parameter monitoring need in core while being minimally intrusive in the reactor core. Detector designs proposed herein can monitor fuel compression and expansion in both the radial and axial dimensions as well as monitor linear power profiles and fission rates during the operation of the reactor. In addition to pressure, stress, strain, compression, neutron flux, neutron spectra, and temperature can be observed inside the fuel bundle and fuel rod using the proposed system. The proposed research aims at developing radiation hard, harsh environment multi-parameter systems for insertion into the reactor environment. The proposed research holds the potential to drastically increase the fidelity and precision of in-core instrumentation with little or no impact in the neutron economy in the reactor environment while providing a measurement system capable of operation for entire operating cycles.

Proposed Scope Description

Significant work has been done over the last few years on the use of nanoparticle based scintillators. This work focused primarily on incorporating new scintillator material nanoparticles into a composite matrix to create large volume scintillators for gamma ray detection. These methods however suffer from the inability to collect the scintillation light. The light is either trapped internally in the nanoparticle, or is lost in scattering/absorption between the nanoparticle, host matrix interface. The idea behind plasmonic cloaking was originally published by Pendry et al. in 2006. These cloaking devices are characterized by:

- Creating a closed space from which electromagnetic radiation is excluded, and the incident radiation is steered around it.
- The application of mathematical transformation on the original space creating a warped space, implemented by spatially varying permittivity and permeability.
- The use of metamaterials to obtain extreme values of permittivity and permeability with strong anisotropy, typically requiring resonating metal elements that limit the device bandwidth.

Through the use of metamaterials, the PIs aim to develop planar neutron detectors and large volume neutron detectors. These detectors will have high efficiencies for neutron detection and will have a high gamma discrimination capability. Each of these components will be described in subsequent sections.

Plasmonic Cloak Theory

Plasmonic cloaking is a method for creating a metamaterial in which light is bent around a highly absorbing material without interacting with the core. A metamaterial is a nanomaterial with an engineered structure of two or more materials which elicits specific phenomena including improved reflection, improved light yields, quantum wells, quantum confined materials, surface plasmon layers, and plasmonically cloaked materials. This bleeding edge technology is taken from the most recent advances in materials science and nanotechnology. In cloaking, the light is bent around the central core of arbitrary shape by designing a specially engineered structure to surround the core. This specially engineered structure is designed to have a low or negative permittivity. The intrinsic robustness of this system can be designed for a band of wavelengths. These methods have been demonstrated in several

different applications including random orientations and clusters of various dielectric and conducting objects. This method has been successfully used to hide or cloak an object in a two dimensional array. The PIs have demonstrated this technology by producing this two dimensional structure.

Neutron Detection Using Metamaterials

Simulations and fabrication of a novel neutron detector material has begun by the PIs and shows significant promise as a large volume wide energy band neutron detector material. This new detector scheme has high sensitivities to fast neutrons from energies of 20 MeV down to thermal energies. By using cutting edge nanotechnology research, a novel scintillator structure based on metamaterials is being proposed. The detector is designed around a plasmonically cloaked metamaterial. Here, nanoparticles of arbitrary shape are coated through a fluidized bed reactor which the PIs are currently developing. A thin plasmonic layer is used to bend scintillation light around the light absorbing nanoparticle core. Light is no longer scattered by the nanoparticle or trapped inside it's unique facets. A sample calculation showing the plasmonic cloak can be seen in Figure 1. The nanoparticles can be created in bulk, kilogram size batches. ${}^6\text{LiF}$, ${}^6\text{LiCO}_3$ or GdO would be used as the core material. HfO , TiO , ZrO or other high index material would be used in the plasmonic layer. The cloaking layer can be applied through an atomic layer deposition process in a fluidized bed reactor (FBR). Several

designs of scintillator will be considered. The first scintillator type is comprised of a plastic scintillator matrix which has suspended in the matrix a high density of plasmonically cloaked nanoparticles of neutron absorbing materials. This type is ideally suited for producing highly efficient neutron scintillators which do not suffer from light collection problems. The second scintillator design builds on the first scintillator design by producing a multilayered metamaterial that is cloaked with a plasmonic cloaking layer. This scintillator is cast in an inert ultra violet transmitting matrix. In the first method, the metamaterial is then cast into a plastic scintillator matrix such as BC408 or BC400. This metamaterial is a nanoparticle with a radius of 5-100 nm of ${}^6\text{LiF}$, ${}^6\text{LiCO}_3$ or GdO which is coated with a plasmonic cloak. Through either the (n, α) reaction in ${}^6\text{Li}$ or neutron capture in gadolinium, the charged particle produced by the nanoparticle easily passes through the plasmonic cloak and deposits 98% of its energy in the plastic scintillator. This design is shown in Figure 2. The light generated in the scintillator is produced isotropically. As opposed to striking another nanoparticle, the light wave interacts quantum mechanically with the plasmonic cloak. In doing so, the light bends around the opaque particle and continues on its original path without loss or scattering. Due to the low absorption in the scintillator matrix, large volumes of scintillator are possible with no noticeable loss in light collection.

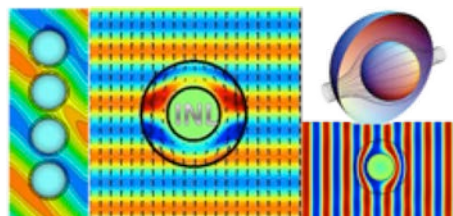


FIGURE 1 - NATURE OF CLOAK

On the left is an array of cloaked spheres. The wave forms do not deform or get scattered by the spheres themselves, which are absorbing.

The center image is a close up of the simulation. Each particle was simulated as a GdO nanoparticle of 145 nm and a 15 nm plasmonic cloak of TiO . On the right are field lines of the light bending around the nanoparticle showing the arbitrary nature of the cloak.

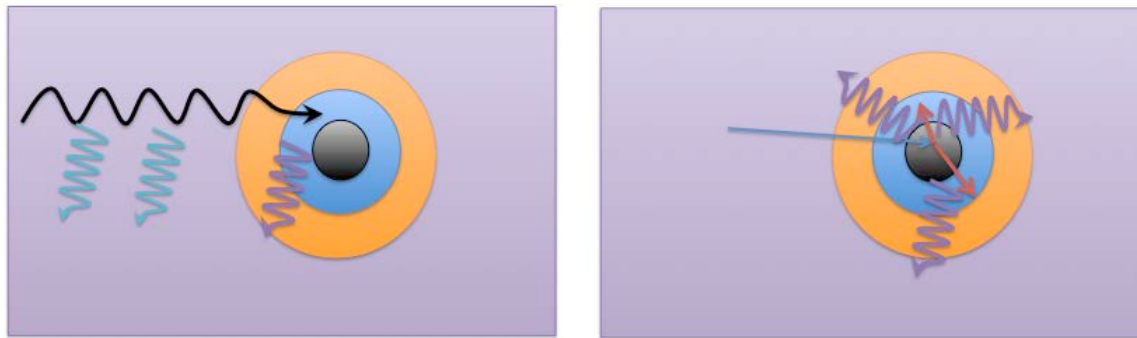


FIGURE 2 - DESIGN OF NEUTRON VERSUS GAMMA DISCRIMINATION FOR DESIGN ONE

THE ORANGE LAYER IS THE PLASMONIC CLOAK, THE BLUE LAYER IS THE SCINTILLATOR LAYER MADE FROM ZNO, THE KERNEL IS MADE FROM ^6Li PURPLE IS A SCINTILLATOR MATRIX. GAMMA RAYS SHOWN ON THE LEFT PRODUCE BOTH SCINTILLATION WAVELENGTHS, WHILE NEUTRONS ONLY PRODUCE ONE SCINTILLATION WAVELENGTH.

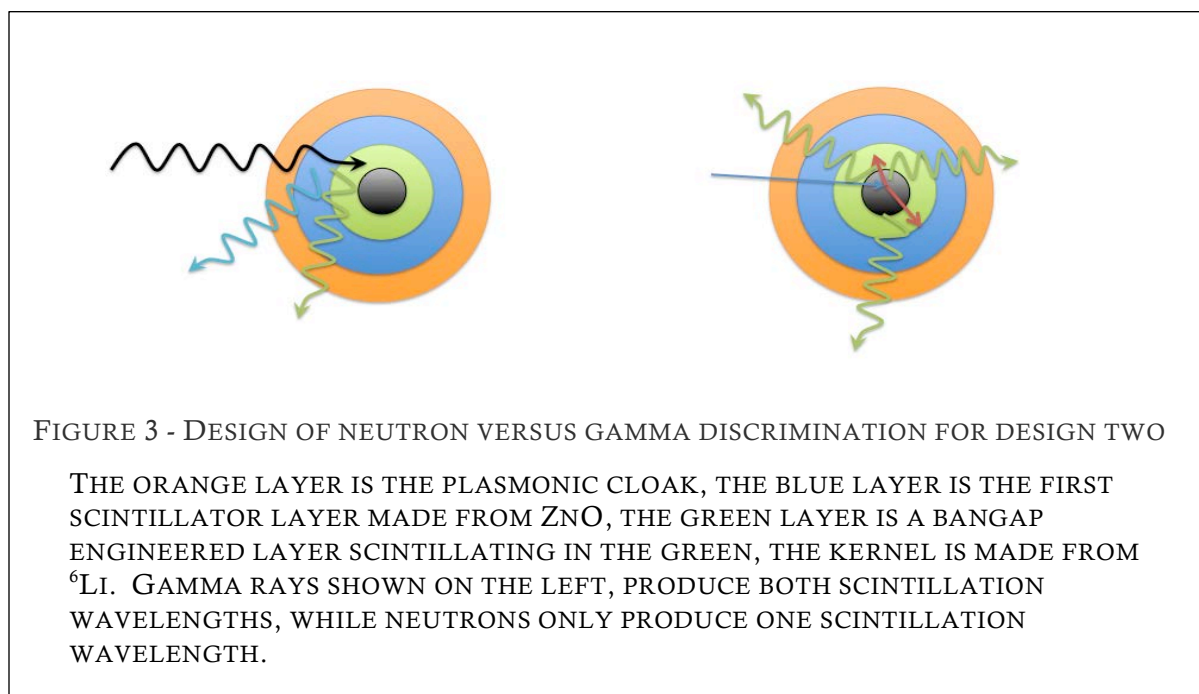


FIGURE 3 - DESIGN OF NEUTRON VERSUS GAMMA DISCRIMINATION FOR DESIGN TWO

THE ORANGE LAYER IS THE PLASMONIC CLOAK, THE BLUE LAYER IS THE FIRST SCINTILLATOR LAYER MADE FROM ZNO, THE GREEN LAYER IS A BANGAP ENGINEERED LAYER SCINTILLATING IN THE GREEN, THE KERNEL IS MADE FROM ^6Li . GAMMA RAYS SHOWN ON THE LEFT, PRODUCE BOTH SCINTILLATION WAVELENGTHS, WHILE NEUTRONS ONLY PRODUCE ONE SCINTILLATION WAVELENGTH.

In a second method, the metamaterial is cast into an inert ultraviolet transmitting plastic matrix. The matrix is no longer the scintillator. The nanoparticle kernel is still a nanoparticle with a radius of 5-100 nm of ^6LiF or $^6\text{LiCO}_3$ which is then coated with a 10 μm scintillator material with a long wavelength in the blue, coated with a second scintillator of 10 μm which scintillates in the near ultraviolet, and then coated with a plasmonic cloak layer. In this configuration, the resulting charged particles (the alpha and the triton) produced from the (n,α) reaction in ^6Li range out in the first scintillator. This scintillator produces a blue wavelength light pulse. The next scintillator layer is transparent to the blue wavelength and thus it passes out of the metamaterial nanoparticle and into the inert matrix. However, when gamma rays interact in the material, they interact by producing recoiling electrons or photoelectrons. These electrons' range is significantly larger than the metamaterials. This will produce both blue and near-

ultraviolet light pulses. The plasmonic cloak will prevent the light from interacting with the other nanoparticles in the matrix. For a neutron only event, light pulses in the blue are the only scintillations to be produced. In gamma ray events, blue and ultraviolet light pulses are produced. A coincidence system can be used to provide the neutron versus gamma discrimination. By having two different sensitive PMTs or APDs one for blue, one for ultraviolet and blue, the two signals can be compared and run in anti-coincidence mode. This method is shown in Figure 3.

This scintillator design is sensitive to both fast and thermal neutron fields. This unique solution can easily obtain 100% efficiency for thermal neutrons and absolute efficiencies in excess of 50% for fast neutrons. Fast neutron scintillators can run in two different modes. The first is a capture gated method. This is possible due to the hydrogen content of the plastic scintillator or the inert UVT matrix. The neutrons thermalize in the scintillator and are captured producing a large light pulse. This method is usually considered capture gated neutron spectroscopy and is shown in Figure 4. Neutron versus gamma discrimination can be achieved by utilizing a third configuration for the metamaterial including the plasmonic cloak. This configuration has three distinct scintillators, and a neutron absorbing kernel. Recoiling protons interact in only the outer layer scintillator, scintillating in the UV. The middle layer scintillates in the blue, and is out of the range of the charged particles produced from the central kernel or the recoiling protons. The inner kernel charged particles interact in the inner scintillator which scintillates in the green. By using a three PMT or APD light collection system, each one sensitive to a narrow band of scintillation wavelengths, and by coincidence, the signals, neutron versus gamma discrimination can be achieved and even discriminate between fast and thermal neutrons. Thermal neutron only events would scintillate in green, Fast neutrons would scintillate in the UV, whereas the gamma events would scintillate in green, blue and UV. This three-wavelength method can achieve theoretical neutron versus gamma discrimination levels of 10^6 .

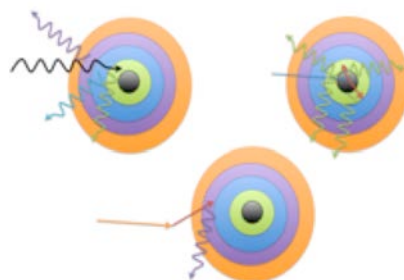


FIGURE 4 - DESIGN OF NEUTRON VERSUS GAMMA DISCRIMINATION FOR DESIGN THREE

DESIGN THREE INCORPORATES FAST NEUTRON RESPONSE. THE ORANGE LAYER IS THE PLASMONIC CLOAK, THE BLUE LAYER IS THE FIRST SCINTILLATOR LAYER MADE FROM ZNO, THE GREEN LAYER IS A BANGAP ENGINEERED LAYER SCINTILLATING IN THE GREEN, THE KERNEL IS MADE FROM ^6Li . GAMMA RAYS SHOWN ON THE LEFT, PRODUCE BOTH SCINTILLATION WAVELENGTHS, WHILE NEUTRONS ONLY PRODUCE ONE SCINTILLATION WAVELENGTH. PROTON RECOIL EVENTS ONLY INTERACT IN THE OUTER REGION, SHOWN ON THE BOTTOM CARTOON.



FIGURE 5 - DESIGN OF NEUTRON VERSUS GAMMA DISCRIMINATION FOR DESIGN THREE (NO KERNEL)

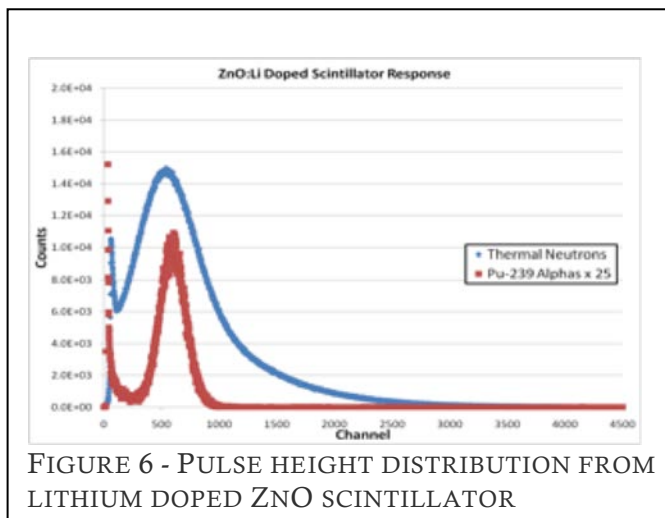
DESIGN THREE INCORPORATES FAST NEUTRON RESPONSE. THE ORANGE LAYER IS THE PLASMONIC CLOAK, THE BLUE LAYER IS THE FIRST SCINTILLATOR LAYER MADE FROM ZNO, THE GREEN LAYER IS A BANGAP ENGINEERED LAYER SCINTILLATING IN THE GREEN. IN THIS DESIGN THERE IS *NO KERNEL*. GAMMA RAYS SHOWN ON THE LEFT PRODUCE BOTH SCINTILLATION WAVELENGTHS, WHILE NEUTRONS ONLY PRODUCE ONE SCINTILLATION WAVELENGTH. PROTON RECOIL EVENTS ONLY INTERACT IN THE OUTER REGION, SHOWN ON THE BOTTOM CARTOON.

The second fast neutron scintillator resembles the traditional fast neutron scintillator method. Here, only fast neutrons would interact with two different scintillators. The central kernel of neutron target nuclei has been removed, and replaced with a scintillator. The plasmonic cloak keeps the scintillators from reabsorbing their own scintillation. Neutrons would produce only UV scintillations while gammas produce both blue and UV. This method is shown in Figure 5.

To further improve the detector performance, an anticoincidence system will be created by segmenting the detectors. With anticoincidence system, the detector becomes fairly insensitive to room return and scattered neutron contributions.

This will further improve the detector response and the spectroscopic resolution of the detector system.

The low energy component of the detector array will be comprised of doped ZnO scintillators. The doped scintillators show excellent neutron versus gamma discrimination and can be grown in large planar arrays. These scintillators can use the shift in the (n, α) peak from ${}^6\text{Li}(n, \alpha)$ reactions to ascertain the incident neutron energy. This fills the neutron detection gap between 500 keV and thermal neutron energies where many detection systems cannot perform.



Fluidized Bed Reactor Design

The fluidized bed reactor design is not a novel concept. The adaption to be an atomic layer deposition system is, however. The fluidized bed reactor takes and converts a bed of solid particles into a liquid-like substance. This is accomplished through very specific gas flow rates through the nanoparticle media. The system is comprised of many mass flow controllers as well as reactant gas mass flow controllers. Like an ALD system, half cycle, self-limiting pulses of gas deposit one half of the two component material on the surface. The fluidized bed is needed to ensure uniform coating of the nanoparticles. A sample design of the fluidized bed reactor is shown in Figure 7. To prevent conglomeration of the nanoparticles, a combination of vibration, mixing and ultrasonic perturbation is used to keep the nanoparticles from clumping during growth.

The PIs have extensive experience in growth of these novel neutron scintillator materials and have a diverse background in materials science, nanotechnology and nuclear engineering with numerous years specializing in neutron detection. The PIs have grown novel plasmonic cloak materials before and have successfully demonstrated the

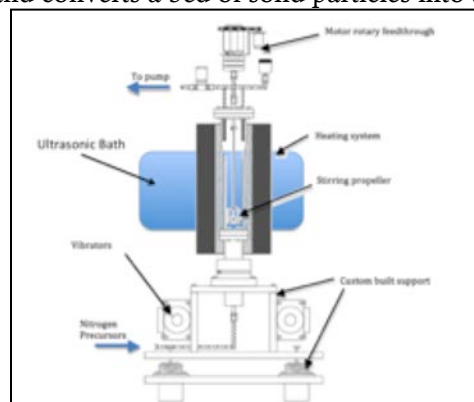


FIGURE 7 - PROPOSED FLUIDIZED BED ALD REACTOR SCHEMATIC

INCLUDES VIBRATION MOTORS, A MIXER IMPELLER, AND AN ULTRASONIC BATH ARE DESIGNED TO KEEP THE SYSTEM FLUIDIZED.

technology. They currently have a preliminary design for the fluidized bed ALD reactor design for the system.

Design of Large Area Array

The large area array will first be created out of planar devices. As the fluidized bed comes online and is able to produce plasmonically cloaked particles, large area devices will be fabricated. This will take on the shape and configuration similar to the Euroball detector array. The specific design will be finalized while working with the other data groups including the Elastic/Inelastic, Chi-Nu, and Fission TPC projects. Each detector design will be specific to the measurement program it is designed for. The detector array aims to help fill in the gap between traditional thermal neutron scintillators and fast neutron scintillators while maintaining excellent neutron versus gamma discrimination. No complicated electronics or pulse shape discrimination are needed, merely coincidence measurements for rejection of gamma ray backgrounds. The plasmonically cloaked scintillators engineer out the gamma ray response. This system has the potential to produce a highly efficient neutron detection system with cutting edge technology.

Current Status:

Deliverable #1: Document reporting the response of the first planar devices and initial growth quality of new detector system provided to DOE.

Milestone #1: Grow planar device with Distributed Bragg Reflector (DBR) structure

Deliverable #1 (Participants) ISU

Deliverable #1 (Status): A metal oxide chemical vapor deposition tool will be required for later work to mass produce coated nanoparticles. The MOCVD tool heater element was damaged from prolonged storage. A new heater element was fabricated from nichrome sheet. The new sheet was thinner than the previous heater element and localized heating caused the heater element to distort, shorting out. A new heater element was designed in Solidworks© and was fabricated. The new heater element is now installed and has not produced any adverse results. The preliminary water permit has been issued and the tool has begun to grow new materials. Base runs to determine the correct mass flow rates are being conducted. This has been completed and presented at ANS.

Deliverable #2: Document reporting the response of the first band gap engineered sample devices and initial growth quality of new detector system provided to DOE.

Milestone #2 Grow band gap engineered scintillators

Deliverable #2 (Participants) ISU

Deliverable #2 (Status) Models were completed of two different photonic crystal designs for the ZnO/LiF scintillator. One photonic design is a Modified Bragg Reflector (MBR), because it consists of alternating thin films of ZnO and LiF, and can be seen in [Figure 1](#). The MBR design poses a modeling challenge for several reasons. First, the MBR design will always have an odd number of layers because one additional layer of ZnO will always be necessary to capture all secondary charged particles resulting from Li-6 capturing neutrons. That a MBR photonic scintillator must have an odd number of layers renders the MBR scintillator a non-periodic photonic structure and breaks the discrete symmetry through the thickness of said scintillator, if all ZnO thin-films have the same thicknesses. Quarter-wave stacks and other Bragg reflector or Bragg fiber geometries have an overall even number of layers. The necessary periodicity and hence, the symmetry can be restored if the thickness of the middle ZnO layer is doubled.

The dielectric contrast over the entire thickness of this MBR scintillator can be mathematically described by a Fourier series. A challenge in modeling this MBR design in the code MIT Photonic Bands (MPB) has been coding in the dielectric contrast function as a function of position into the MPB input control files, and this remains an ongoing process. The Fourier series expansion for this MBR scintillator is

$$n^2(z) = a_0/2 + \sum_{one}^{\infty} [a_m \cos\left(\frac{m\pi z}{L}\right) + b_m \sin\left(\frac{m\pi z}{L}\right)]$$

$$a_0 = n_{ZnO}^2 - \left[\frac{(z_4 - z_3) + (z_2 - z_1)}{L}\right](n_{ZnO}^2 - n_{LiF}^2)$$

$$a_m = -\left(\frac{n_{ZnO}^2 - n_{LiF}^2}{2m\pi}\right) \left[\left(\sin\left(\frac{m\pi z_4}{L}\right) - \sin\left(\frac{m\pi z_3}{L}\right) \right) + \left(\sin\left(\frac{m\pi z_2}{L}\right) - \sin\left(\frac{m\pi z_1}{L}\right) \right) \right]$$

$$b_m = -\left(\frac{n_{ZnO}^2 - n_{LiF}^2}{2m\pi}\right) \left[\left(\cos\left(\frac{m\pi z_4}{L}\right) - \cos\left(\frac{m\pi z_3}{L}\right) \right) + \left(\cos\left(\frac{m\pi z_2}{L}\right) - \cos\left(\frac{m\pi z_1}{L}\right) \right) \right]$$

where z_1, z_2, z_3 , and z_4 correspond to the ZnO/LiF interface, L corresponds to the thickness of the MBR scintillator, and $n^2(z)$ corresponds to the dielectric contrast through the axial volume of the scintillator.

The second photonic scintillator that was modeled in MPB was a two dimensional slab. This scintillator consisted of three layers of material: a layer of lithium niobate that was sandwiched in between layers of zinc oxide. Lithium niobate was ultimately chosen as the neutron converter for this scintillator because its refractive index is less than 1% different from that of zinc oxide. The assumption underlying this simulation was that the small mismatch in refractive index is not sufficiently large to distort the symmetry of the photonic crystal. Both square and triangular lattices of rods were modeled. In MPB, all lengths and thicknesses are taken to a relative lattice value, which was set to 368 nm in these simulations; 368 nm is the de Broglie wavelength corresponding to the ZnO band-gap energy of 3.37 eV. A variety of rod diameters were modeled also. The MPB models showed that only a square lattice of air holes yielded any appreciable photonic band-gap, which was a TM-like band-gap of 13.34% between the first and second TM-like modes. The TM-like band-gap reached its maximum value when the hole radius was 184 nm (which is the de Broglie wavelength corresponding to half of the ZnO band-gap energy). Air was the only material that yielded any photonic band-gap.

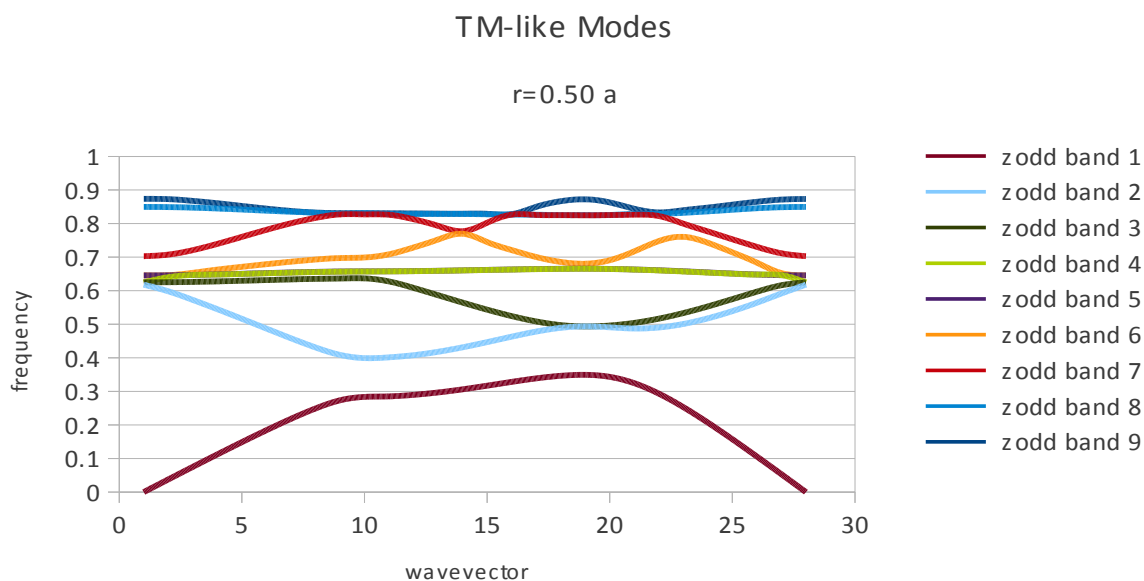


FIGURE 8 - TM-MODE: 13.34% BAND GAP

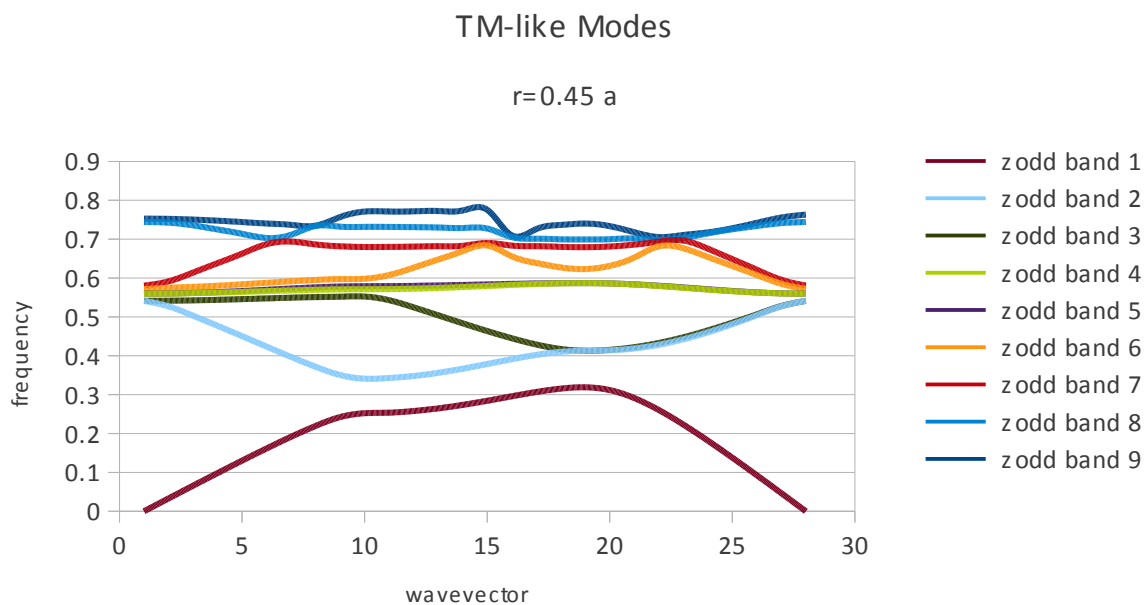


FIGURE 9 - TM-MODE: 6.71% BAND GAP

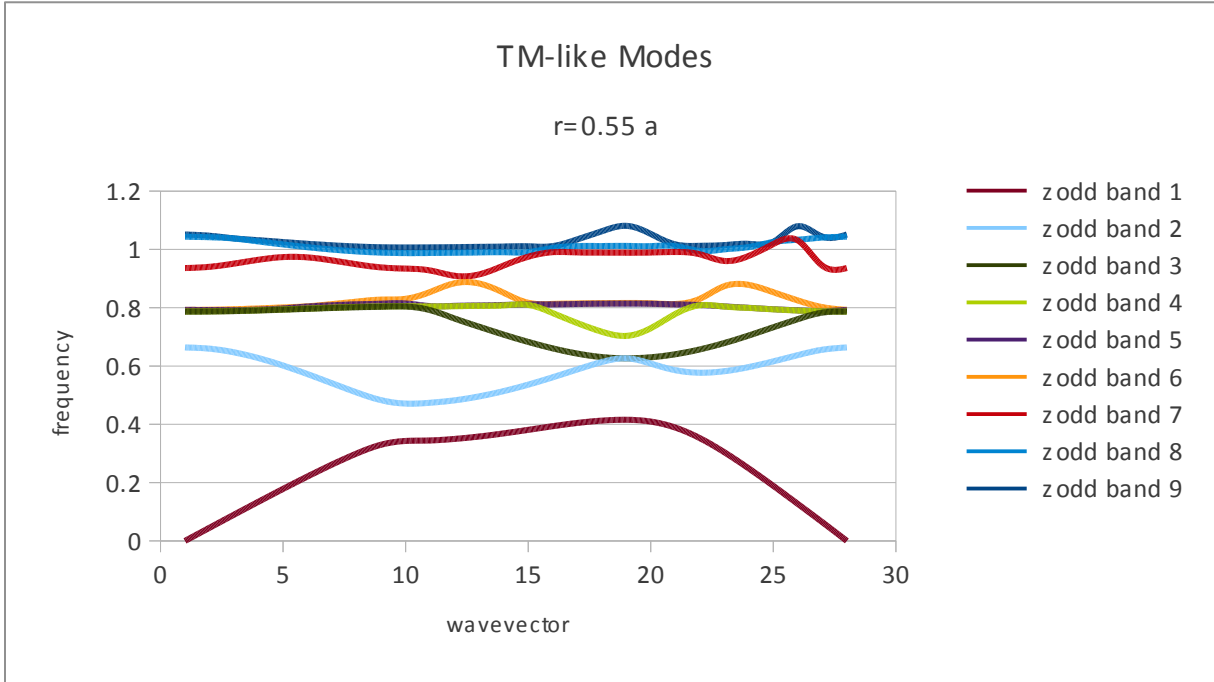


FIGURE 10 - TM-MODE: 12.53% BAND GAP

Additionally, investigations into whether the thickness of a LiNbO₃ neutron converter would affect the photonic properties of this scintillator. The MPB results indicate that the LiNbO₃ thickness does not significantly affect the photonic properties of the slab scintillator. This result is consistent with the assumption that because the refractive indexes of ZnO and LiNbO₃ are very similar, that the photonic slab essentially has the same refractive index.

Shown here are two photonic slab scintillators: one having a LiNbO3 thickness of 166 nm (0.45×638 nm), and the other slab having a thickness of 1.84 μm (5 times 368 nm).

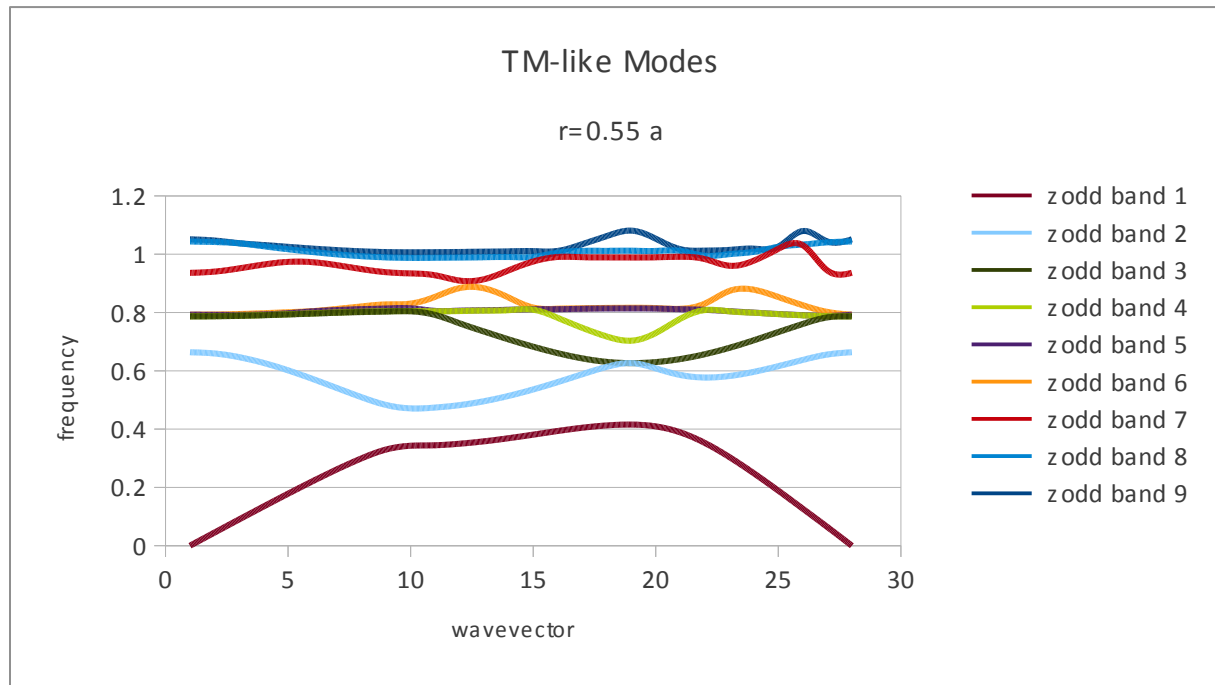


FIGURE 11 - TM-MODE: 13.34% BAND GAP

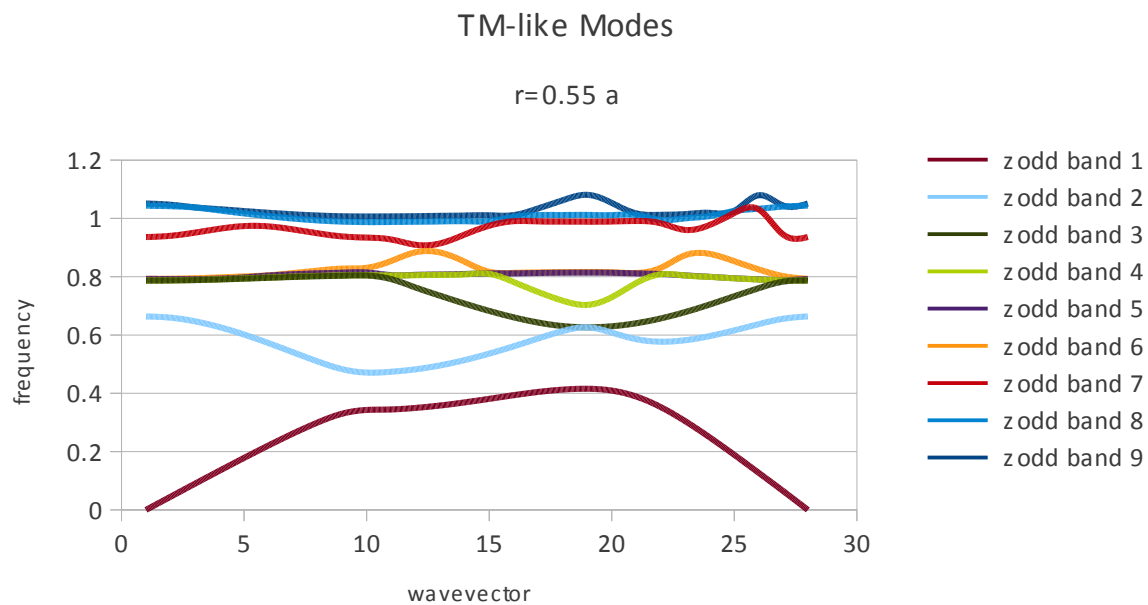


FIGURE 12 - TM-MODE: 13.34% BAND GAP

The modeling of a Plasmonic cloak has been one of the challenges due to its complex nature. MEEP was used by previous investigators to produce working simulations for such a device and is being used to redesign the previously proven cloak at with a visible wavelength of light. Currently the models for various cloak structures are progressing in an effort to maximize efficiency and match the milling capabilities that have so far been demonstrated using the FIB. Several advances in ion milling were made this quarter. This included the incorporation of image guided milling of the nanofeatures.

This deliverable was completed and results presented at ANS.

Deliverable #3 Document reporting first neutron sensor performance.

Milestone #3: Test new scintillators in neutron fields

Deliverable #3 (Participants) ISU

Deliverable #3 (Status) Complete. Tested in reference neutron fields. Presentation to be forthcoming at ANS meeting.

Deliverable #4 Document reporting the optimized response of the first planar neutron devices and initial growth quality of new detector system provided to DOE

Milestone #4: Optimize planar detector design for low energy neutron measurement

Deliverable #4 (Participants) ISU/INL

Deliverable #4 (Status) Complete.

Deliverable #5 Document reporting the commissioning of the reactor data for the first cloaked devices

Milestone #5: Commission fluidized bed reactor

Deliverable #5 (Participants) ISU/Georgia Tech

Deliverable #5 (Status) Design modifications to the Fluidized bed reactor are still ongoing. The design is being simplified in order to limit the number of moving parts and through ports into the vacuum chamber. Some preliminary fluid modeling on the gas diffusion plate was conducted, but the results were inconclusive and a more detailed model will have to be conducted when CFD software becomes available. This is complete.

Deliverable #6 Begin to develop first cloaked devices

Milestone #6: Document reporting the first cloaked nanoparticle tests developed.

Deliverable #6 (Participants) ISU

Deliverable #6 (Status) Research has been conducted for various nanoparticles and the possibility of growing them versus ordering them. This has been generally unproductive since a cost analysis of this method would require a detailed knowledge of the process for an individual particles creation. ZnO is the easiest and while several papers detail the process the exact numbers are generally withheld for the purpose of proprietary uses. This does not preclude possibility of nanoparticle production it just suggests that much experimentation will be required to perfect a process for personal use. Currently a variety of nanoparticles have been purchased. These include: aluminum oxide, zinc oxide, magnesium oxide, tungsten oxide, zirconium oxide, barium titanate, silicon carbide, and boron nitride. We are currently in the process of characterizing these nanoparticles.

Before receiving nanoparticles, first the glove box had to have maintenance and hookup conducted on it. After it was successfully plumbed with nitrogen and had a vacuum pump operating it was safe to transfer the ordered nanoparticles into storage containers as well as onto scanning electronic microscope (SEM) stems for observation. Currently, measurements are being conducted on a sample of each nanoparticle to gain insight into the actual size range of these nanoparticles using the SEM. Ongoing has been preliminary setup for the arrival of the Focused Ion Beam (FIB) which will ship at the end of April with training to be conducted in May. The FIB will allow the creation of lattice structures with customizable lattice spacing based on the way the script program is written. Some preliminary development of sample scripts has been conducted as well.

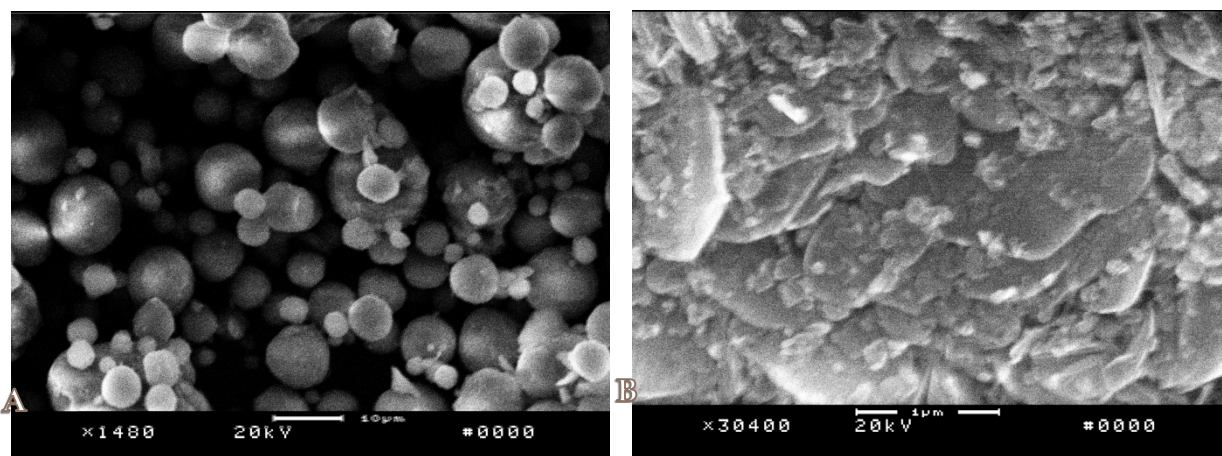


FIGURE 13 - PRELIMINARY SEM IMAGES OF: A) Al_2O_3 AND B) BN

The installation of multiple instruments associated with the project has been the primary focus for the past months. In addition to the physical installation additional infrastructure has to be setup for the equipment as well. This included additional nitrogen and air lines as well as a water cooling system for the TEM. The focused ion beam microscope has been up and running since the end of May and already extensive milling experience has been gained. With the assistance of other students milling tests have been conducted on the various shapes and structures that are achievable with this model of equipment. From the tests conducted a reactive ion etch seems to be the ideal method for creating the Plasmonic cloak structures that will need to be replicated from previously performed work. This work will be expanded upon and the frequency of the cloak will be changed to be optimized for the emission wavelength that is expected inside the coated nanoparticles.

With the installation of a transmission electron microscope within the last two weeks, the resolution of nanoparticles that can be characterized has been greatly increased. With a 4nm resolution extremely fine particles can be characterized. This process has already begun and fairly

large variations are being seen in the sample grids. This could be a problem when the atomic layer deposition device is created since a uniform particle density will be required by the cloak to bend the light uniformly around the detection cores of the particles. This could easily be overcome by utilizing a consistent in-house manufacturing process with much less variation in particle diameter. Preliminary investigation into manufacturing processes for nanoparticles is currently underway for ZnO.

In order to acquire particles size measurement averages a minimum of two sample grids of each type of nanopowder were prepared on carbon film mesh grids for the transmission electron microscope. From each of these prepared samples the investigator attempted to identify individual particles from the sample masses. Multiple methods for sample preparation were endeavored to minimize agglomeration of particles to ensure accurate size measurements. The first method was an alcohol solution with the desired particle. This was suggested by the technician who installed the TEM. This had limited success since the solution when applied to the grid still resulted in particle clumps. This method was also tried with an additional drying period before analysis but again resulted in similar results. The most successful method used was a dry powder preparation applied directly to the grid. This required little prep work and only need a very tiny application of the powder to ensure only a thin layer was applied.

Once the grid preparation method was standardized, the investigators introduced the samples into the TEM for analysis. With the extremely high magnification provided by the TEM very accurate measurements could be taken of the individual particle diameters. The particle diameters range from 800 nanometers down to approximately 10 nanometers. Images of the measurements using the TEM can be seen below in figure 10. Due to the particles being manufactured out of house many show inconsistent size variation and would be less than ideal for the purposes of the project. The full analysis of the individual particles can be found in the attached excel documents as well as images of the measurements that were performed during analysis.

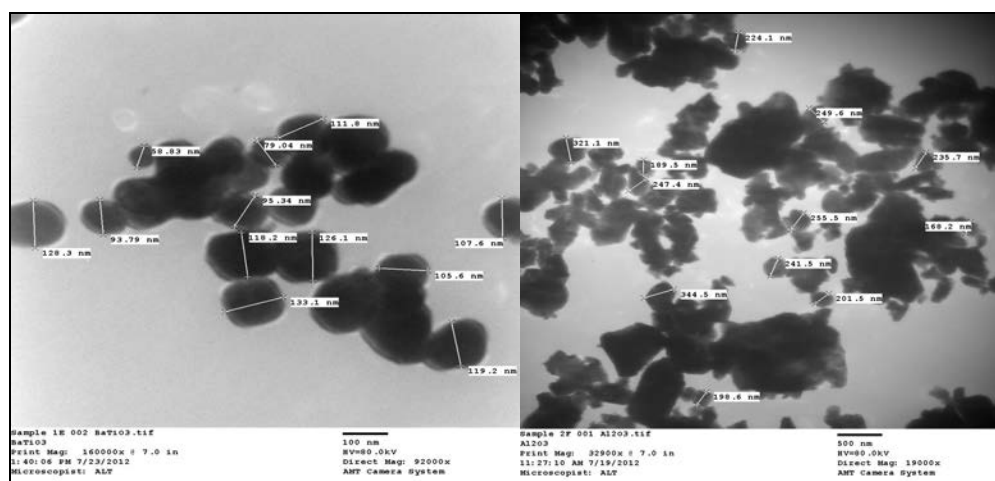


FIGURE 14 - TEM MEASUREMENT IMAGES OF: A) BaTiO_3 B) Al_2O_3

The installation of additional equipment has continued through the past months and we are now fully operational in the microscopy lab. The STEM has been fully installed and the advanced training meeting is currently being scheduled so that we can use the FIB to create TEM

samples. The STEM is another high resolution electron microscope capable of observing the graphitized carbon lattice (.34 nm) and gold lattice (.26 nm) structure. The STEM also has 3 different types of sample holders. There is a standard holder that can be used to image on standard 3mm TEM samples as well as an adaptive holder that allows secondary electron imaging of bulk samples. There is also a heated sample holder and a cryogenic sample holder that can be used to image at reasonably high magnification the effects of temperature on various samples. The STEM also required the calibration of the camera system since it is set some distance from fluorescent screen. This made the magnification of the camera inaccurate and needed a correction factor to determine the true magnification of the images taken. The correction factor for the camera system was 5.3, thus the images taken are actually 5.3 times the magnification stated by the software. There have been some preliminary images taken showcasing the STEMs resolution and for training purposes. Micromanipulators have also been installed in an optical microscope setup to allow for the extraction of samples prepared in the FIB permitting for x-ray diffraction of bulk samples.

A manufacturing process for the aqueous growth of ZnO has been acquired and is currently under investigation. The production and testing of the ZnO process is now made possible with the recent acquisition of the proper chemicals and a furnace. A new chemical wet lab is being setup for the chemical experimentation required to refine these processes. Further testing of the process will be required to determine how effectively the process can be used growth of nanorods in a predetermined template. To assist in this process of testing a new optical lab has been setup by the investigators. The optical lab will serve as a testing ground for a variety of optical experiments needed to test the productions of the investigators experiments.

The aqueous growth process for zinc oxide was accomplished using techniques similar to [1]¹ which used a one to one molar ratio of zinc nitrate and hexamethylenetetramine. While the molar ratio is a constant, the concentration is variable. This allowed for adaptable densities across the surfaces of the materials on which the zinc oxide was being grown. Multiple concentrations were demonstrated using this method and resulted in a variety of features being seen on the surface of a sapphire substrate. For the aqueous growth of zinc oxide to be fully understood a combination of time, temperature, and concentration must be mapped out to produce repeatable, controlled results. The investigators are currently in the process of mapping this three dimensional phase space.

[1] ¹ S. Xu, Z.L. Wang, "One-Dimensional ZnO Nanostructures: Solution Growth and Functional Properties" Nano Res, DOI 10.1007/s12274-011-0160-7

Some of the preliminary results from this phase space mapping have shown promise for using this technique to eventually make both the metamaterial cloak as well as the zinc oxide scintillator. Shown below are several images of variable concentrations of zinc oxide that were grown on sapphire. At higher concentrations distinct hexagonal rods were clearly demonstrated. They show random directionality but this may be due to a lattice mismatch with the substrate on which they were grown. The rods will be useful for creating the actual pattern for the metamaterial surface. They just need to be grown in controlled patterns and at much smaller sizes. At lower concentrations very fine structured “bushes” were grown on the surface. These grew from a single nucleation point. The individual growths on these bush-like objects are clearly sub-wavelength features. These are important for the manufacturing of the metamaterial surface that the detector particles will be cloaked in since the rods must be sub-wavelength in size and spacing, according to current models. Another important characteristic that

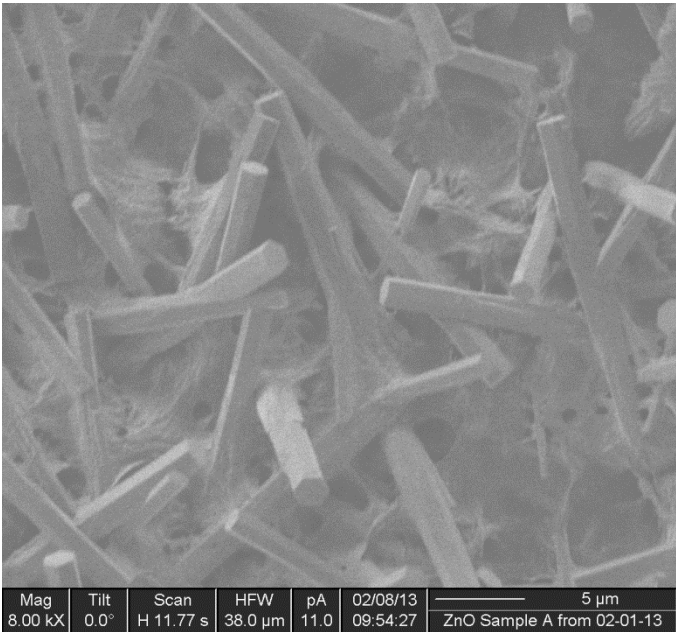


FIGURE 16 - HEXAGONAL ROD GROWTH ON THE SURFACE OF SAPPHIRE. 50MM CONCENTRATION.

has been demonstrated in the aqueous growth on sapphire has been the optical transparency of the zinc oxide layer on the surface. This will be vital for allowing the scintillated light to escape and be counted in the detector system. Finally at a variety of concentrations smooth planar growth of zinc oxide has been observed. This will allow for the zinc oxide scintillators that the particles will be coated in to have a smooth planar surface to construct the cloak upon.

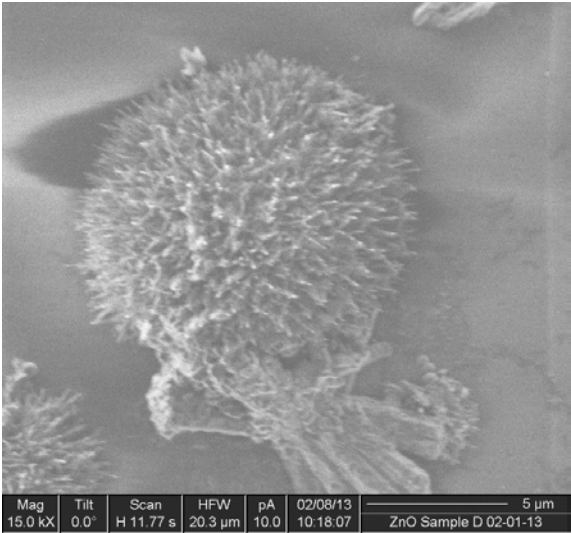


FIGURE 15 - FINE STRUCTURE GROWN FROM SINGLE NUCLEATION SITE ON SAPPHIRE. 20MM CONCENTRATION.

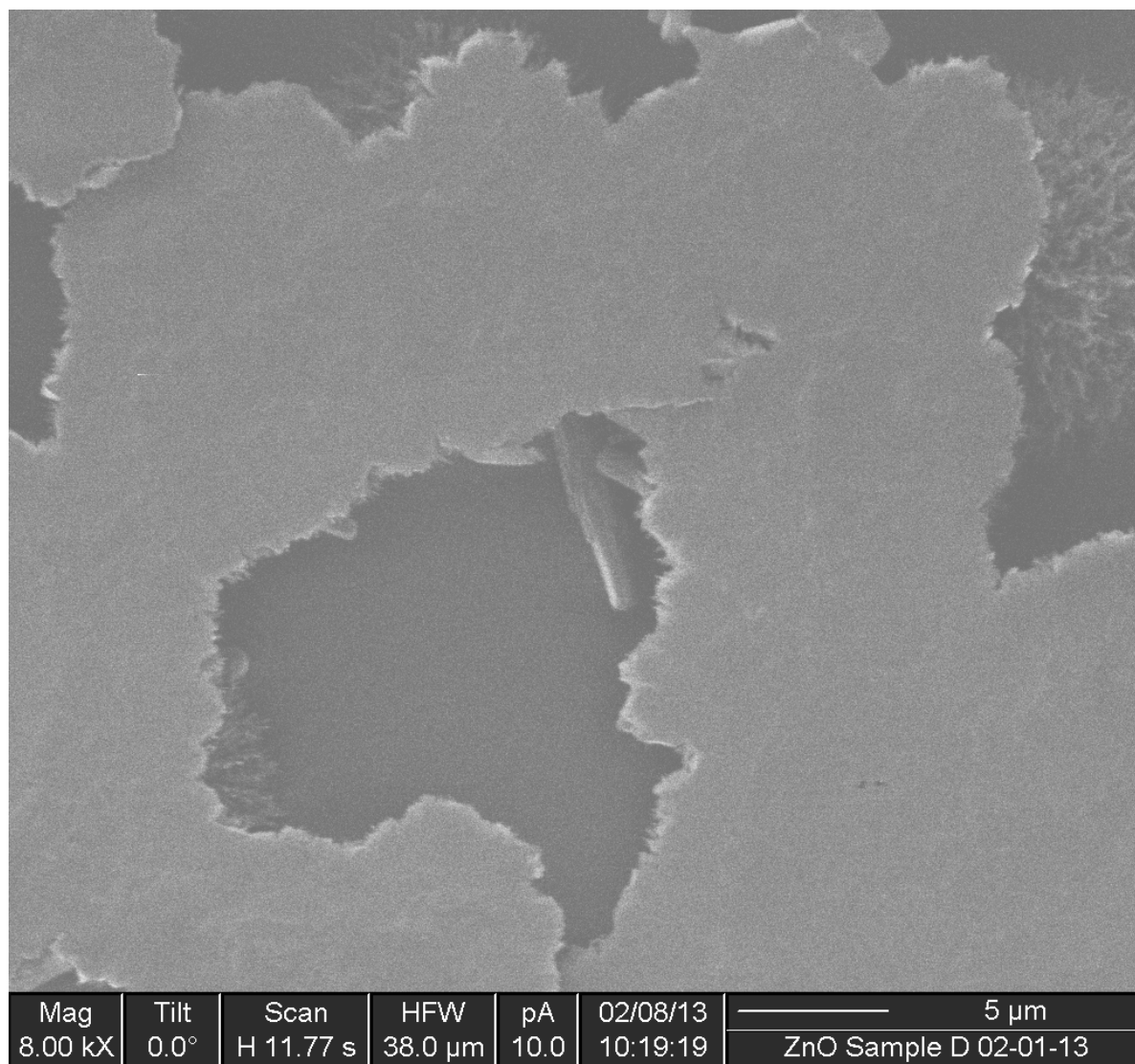


FIGURE 17 - PLANAR ZINC OXIDE GROWTH ON TOP OF FINE STRUCTURES. 20 MM CONCENTRATION

Following the preliminary growth experiments for aqueous zinc oxide growth, the investigators proceeded to map various growth times for a three dimensional phase space. This included a range of concentrations from ten millimolar to fifty millimolar in ten millimolar increments as well as a range of temperatures from fifty to ninety-five degrees Celsius in five degree increments. The time ranges the investigators were primarily concerned with was twelve, twenty-four and thirty-six hours since those times would show if there was residual reactants left in the solutions after longer growth periods. The substrate for these samples was a sapphire disk with pulsed zinc oxide pre-grown with gallium on it to allow for a better lattice match than was originally observed on a pure sapphire disk.

The twenty-four hour growth cycle has been completed by the investigators and their results are currently being analyzed using various techniques that include focused ion beam microscope cross sections as well as XRD analysis. The imaging of these zinc oxide growths has shown some interesting results that include multiple micrometers worth of zinc oxide growth on the surface of some of these

samples. The rods that were seen on the surfaces of some of the samples have been shown to range in diameter and height based on the concentration and temperature. The images below show some of the images used to characterize these rod sizes as well as some of the cross sections that were performed to analyze the depth of the growth that is occurring on these samples.

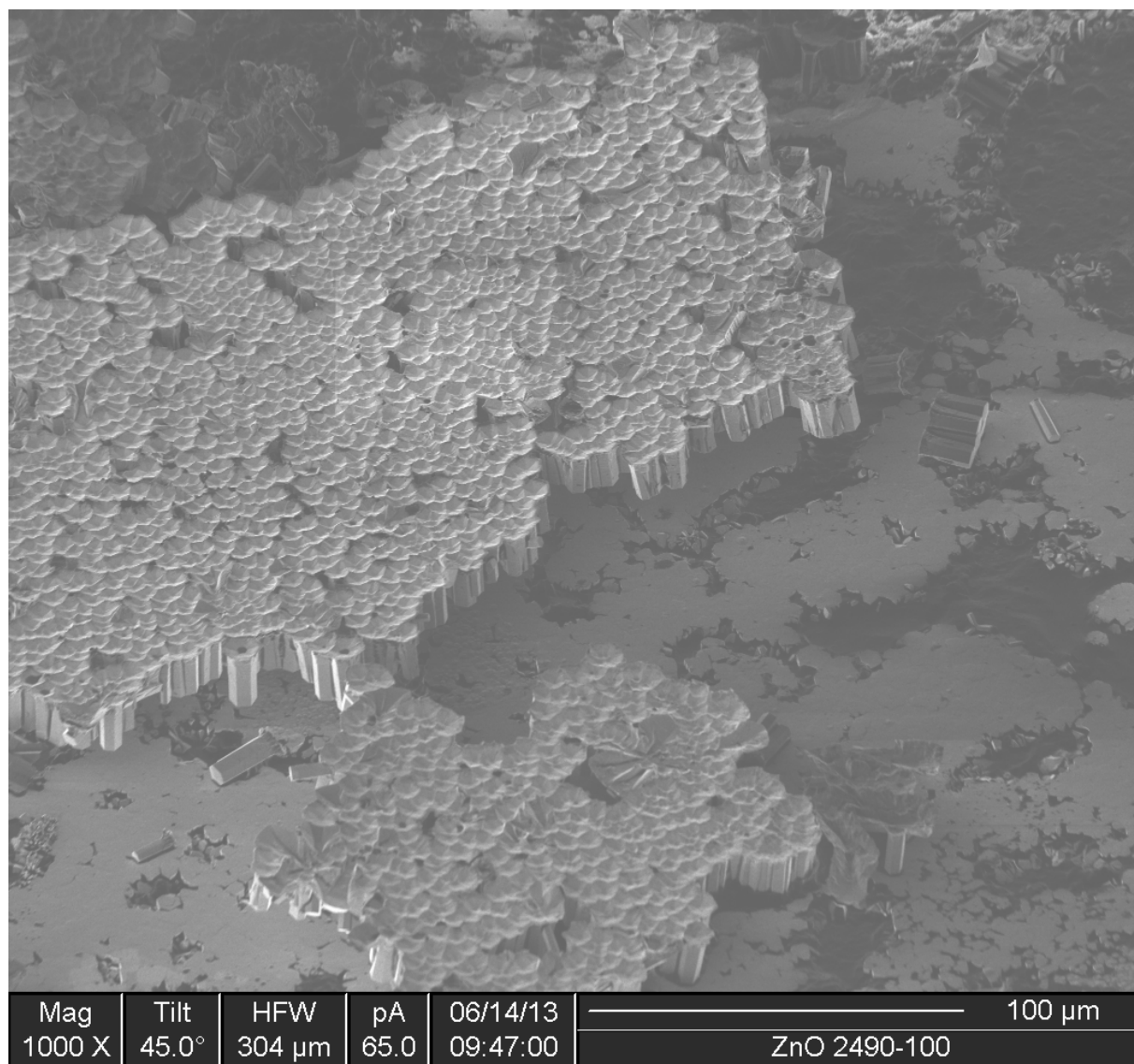


FIGURE 18 - VERTICALLY ALIGNED HEXAGONAL ROD GROWTH ON THE SURFACE OF SUBSTRATE. 100MM EXPERIMENTAL CONCENTRATION

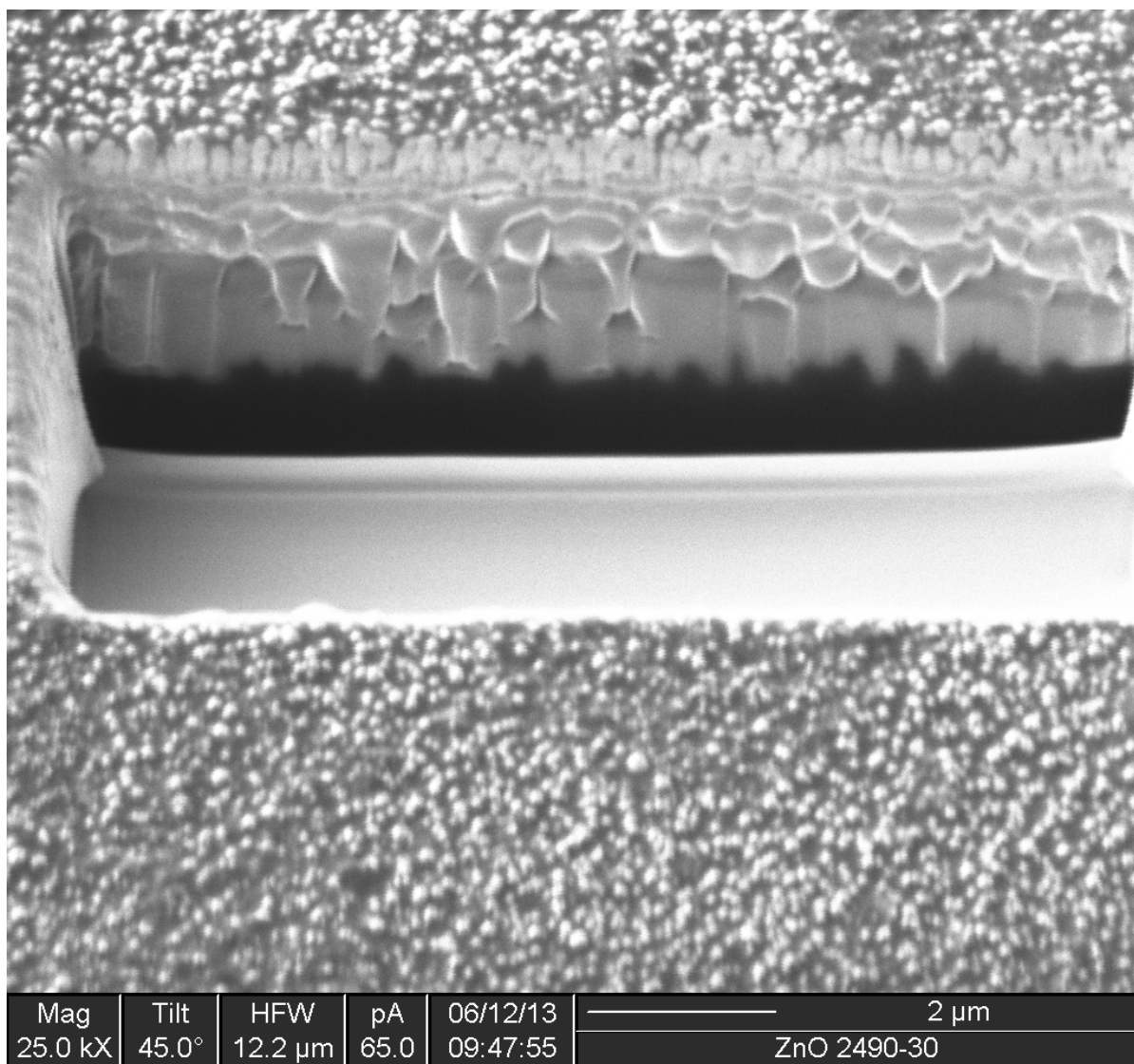


FIGURE 19 - CROSS SECTION ANALYSIS OF A 24 HOUR GROWTH CYCLE AT 90 DEGREE CELSIUS WITH A CONCENTRATION OF 30 MM

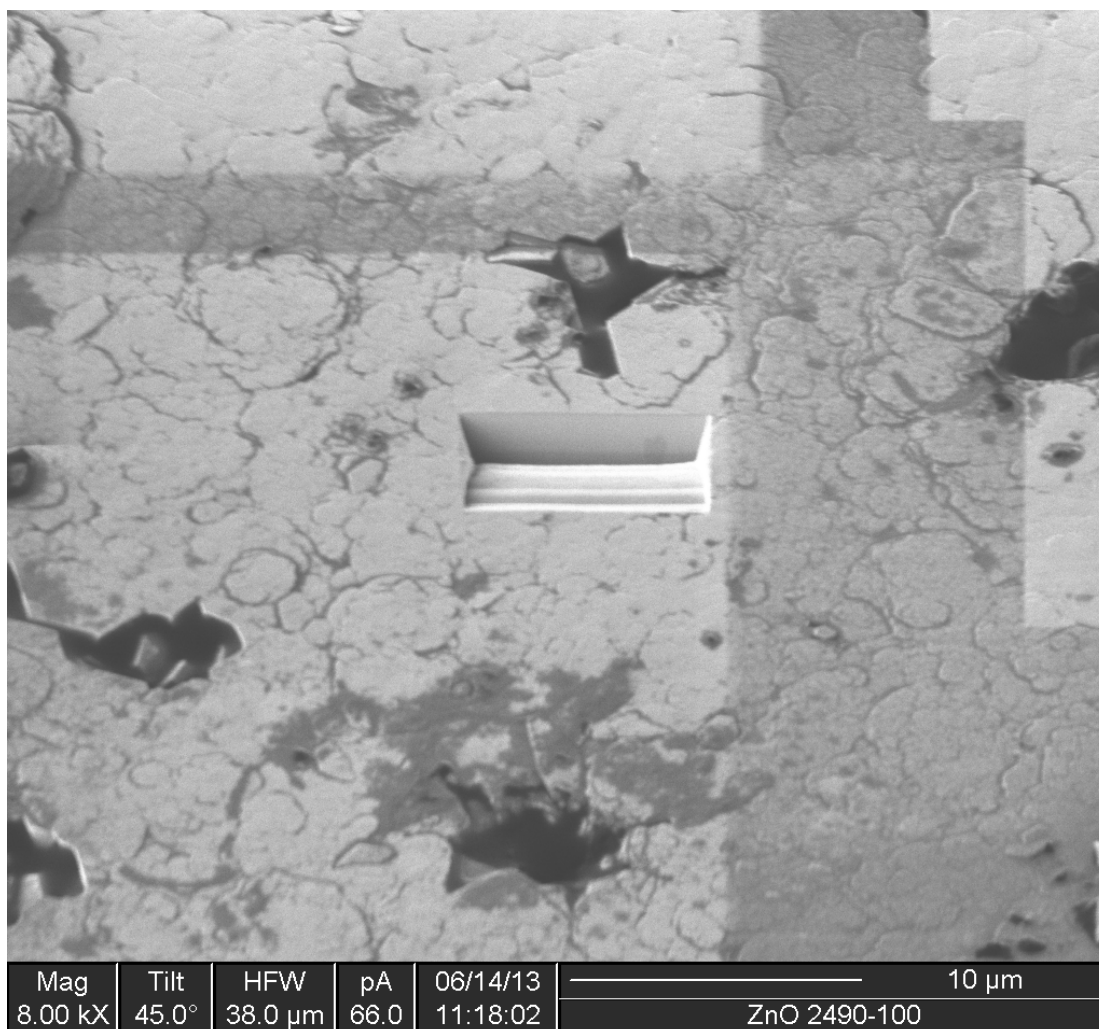


FIGURE 20 - CROSS SECTION OF 24 HOUR GROWTH CYCLE AT 90 DEGREES CELSIUS WITH 100 mM EXPERIMENTAL CONCENTRATION. SHOWS CLEAR DEPTH OF MULTIPLE MICROMETERS OF GROWN ZINC OXIDE ON THE SURFACE OF THE SUBSTRATE

The investigators finished the aqueous growths of zinc oxide for the phase space of interest. This includes growths of twelve, twenty-four, and thirty-six hours at temperature ranges from fifty degrees Celsius to ninety-five degrees Celsius in five degree increments with concentrations from ten to fifty millimolar with ten millimolar increments. The samples are currently being analyzed using electron imaging to characterize the surfaces of these samples. To further the goal of doing this analysis quickly a new imaging program has been implemented to take a series of images of a large field of view. It scans back and forth over the area of a sample taking small high resolution images of an area designated by the user. Then once all the images are collected the investigators can create a mosaic of the area the gives a clear idea of the features present for the sample. Any samples of additional interest will still need to be analyzed further with cross sections taken to provide a more detailed analysis.

The investigators continue to collect imaging data on the 200 samples using a focused ion beam microscope. The mosaic images show more crystalline patterned growth at higher temperatures

generally and more planar growth at lower temperatures. However this data is only for the twenty-four hour growth periods and still needs to be analyzed for the twelve and thirty-six hour growth periods. The upcoming installation of another SEM should expedite the imaging process once its installation is complete.

The electron imaging of all of the samples is complete. The x-ray diffraction work for the 24 hour sample set is also complete and can be seen in Appendix D. The investigators continue to analyze the remaining 12 hour and 36 hour samples using x-ray diffraction. Radiation work has been delayed due to a shortage of parts needed to build the testing chamber for the samples. The work is expected to commence shortly.

The scanning of the 002 peak of the zinc oxide samples has been completed for all data groups. Analysis of the full width half maximum data is underway and shows promising results compared to the baseline samples from Cermet and previous MOCVD grown samples. The appendix D data set has been updated and a naming convention of time, temperature and then concentration is being used. The testing chamber has been completed. The alpha characterization of these samples will begin as soon as a suitable alpha source has been acquired.

This is complete.

Deliverable #7 Document reporting the first cloaked nanoparticle based radiation tests developed

Milestone #7: Test first cloaked scintillators in radiation field

Deliverable #7 (Participants) ISU/GT

Deliverable #7 (Status) The modeling of a Plasmonic cloak has been one of the challenges due to its complex nature. MEEP was used by previous investigators to produce working simulations for such a device and is being used to redesign the previously proven cloak at with a visible wavelength of light. Currently the models for various cloak structures are progressing in an effort to maximize efficiency and match the milling capabilities that have so far been demonstrated using the FIB. One of the primary authors of papers on the subject of plasmonically cloaking was present this week at the research complex and a good deal of insight was obtained from his perspective and experience.

Utilizing this insight a preliminary modeling of a cloaking device has been modeled in MEEP. A baseline model has been created to observe the light interaction with the cloaking structure. Changes to the model will be made to optimize the wavelength of the source and the structure to coincide with projected milling capabilities.

This deliverable is complete and presented at ANS.

Deliverable #8 Document reporting the design and potential performance of proton recoil versions of cloaked nanoparticles developed.

Milestone #8: Design proton recoil based detection system.

Deliverable #8 (Participants) ISU/GT

Deliverable #8 (Status) Complete.

Deliverable #9 Final Report.

Milestone #9: Final Report.

Deliverable #9 (Participants) GT/ISU

Deliverable #9 (Status) Complete.

Deliverable #10 Quarterly reports.

Milestone #10: Final Report.

Deliverable #10 (Participants) GT/ISU

Deliverable #10 (Status) Complete.

Budget Data

Project Complete.

Appendix A – MPB Control File for Photonic Slab Scintillator

The MPB control file for the photonic slab scintillator:

```
; ZnO-LiF.ctl

;

; The fundamental problem is that we have a film of a Li-compound sandwiched between two
ZnO films. Our goal is

; to find a lithium compound that will serve as an optimal neutron converter for a ZnO thin-film
scintillator,

; capable of neutron spectroscopy, and the photonic geometry and parameters that will maximize
light extraction out

; of the scintillator . The idea is similar to that of the lithium Si-diode sandwich detector
developed by Moroni

; et al in 1976.

;

; Explanations of the variables are given underneath their declarations.

;

; Define all material parameters

(define-param eps_ZnO 6.2193) ; ordinarily refractive index (n_o) of ZnO at 368 nm (3.37 eV
band gap energy)

(define-param eps_Li 6.2383) ; refractive index of LiF at ZnO band gap energy (LiF has cubic
lattice.)

; The dielectric constants are taken to be  $n^2$ , where n is the refractive index. The refractive
index for ZnO

; is taken to be 2.49. The refractive data for ZnO is taken from Morkoc and Ozgur, and the LiF
refractive data

; is taken from "Handbook of Optics" published by the Optical Society of America.

;

; Define geometry parameters
(define-param r 0.50) ; radius of holes in LiF slab
(define-param h 2) ; height of LiF slab, along the z-axis, and this height is selected for
; particle ranges
(define-param supercell-h 38) ; height of the entire scintillator, along the z-axis
```

```

; All radii and heights used in this simulation are in units of the 368 nm scintillation wavelength
emitted by ZnO,

; (deBroglie wavelength corresponding to the 3.37 eV band gap energy of ZnO).

;

; Define photonic geometries

;

(set! geometry

(list (make cylinder (material (make dielectric (epsilon eps_ZnO)))

(center 0 0 (* 0.5 h)) (radius infinity) (height (* 0.5 supercell-h)))

; ZnO film above LiF

;

(make cylinder (material (make dielectric (epsilon eps_ZnO)))

(center 0 0 (* -0.5 h)) (radius infinity) (height (* 0.5 supercell-h)))

; ZnO film below LiF

;

(make cylinder (material (make dielectric (epsilon eps_Li)))

(center 0) (radius infinity) (height h))

; LiF neutron converter that is sandwiched in between two ZnO slabs

;

(make cylinder (material air) (center 0) (radius r) (height supercell-h))))

; air holes

;

(define-param k-interp 8)

; interpolates 8 k-points between high symmetry points

(define Gamma (vector3 0 0 0))

(define M (vector3 0.5 0 0))

(define K (vector3 0.5 0.5 0))

```

```

(set! k-points (interpolate k-interp (list Gamma M K Gamma)))

; High symmetry points of the irreducible Brillouin zone for a square lattice of air holes
;

(set-param! resolution (vector3 8 8 8))

; Resolution in terms of # of points/grid. Results in a total computation size of 8 x 8 x 8
;

(set! tolerance 1e-4)
;

(set-param! num-bands 9)

; Number of bands solved for at each k-point. Number should be chosen sufficiently
; large enough for wavelength range of interest.
;

(run-zeven)

; solves Master equation for z-even or TE modes, gap in TE modes for an air in dielectric
; structure
;

(run-zodd)

; solves Master equation for z-odd or TM modes, gap in TM modes for a dielectric in air
; structure
;

;(run-tm output-efield-z)

;(run-te (output-at-kpoint (vector3 0.5 0 0) output-hfield-z))

; Output the electric and magnetic fields' z-component for TE bands at point M)
;

(display gap-list)

```

Appendix B – Images of Current Cloaking Model (MEEP)

The images of the current cloaking model as rendered in MEEP.

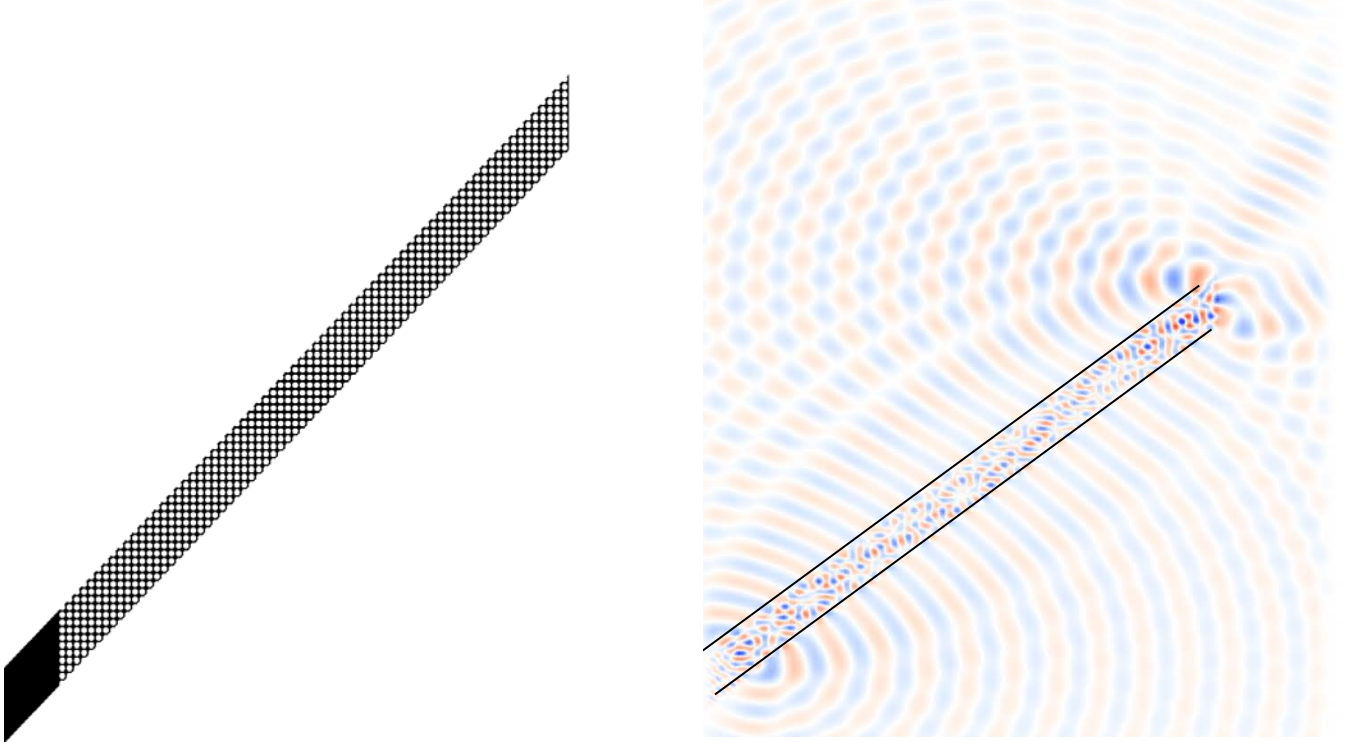


FIGURE 21 - PRELIMINARY IMAGES OF CLOAK MODEL: A) WAVEGUIDE CONTROLLING THE LIGHT SOURCE B) MEEP OUTPUT WITH WAVEGUIDE MARKED FOR REFERENCE

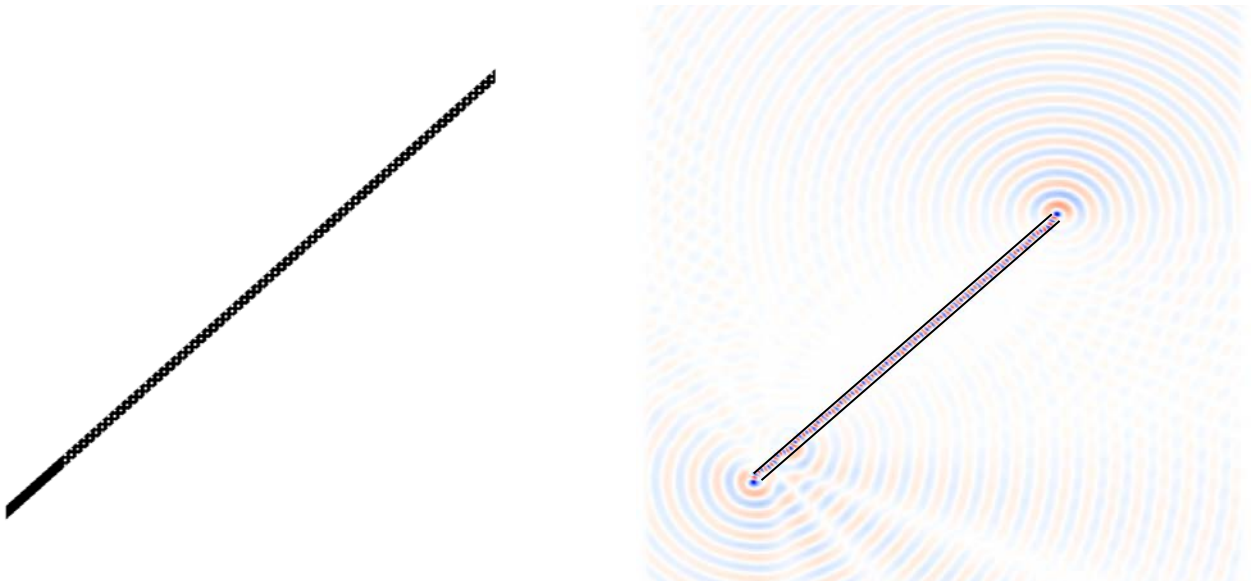


FIGURE 22 - ADDITIONAL MEEP IMAGES: A) SMALLER WAVEGUIDE TO REDUCE INTERFERENCE B) MEEP OUTPUT WITH WAVEGUIDE MARKED FOR REFERENCE

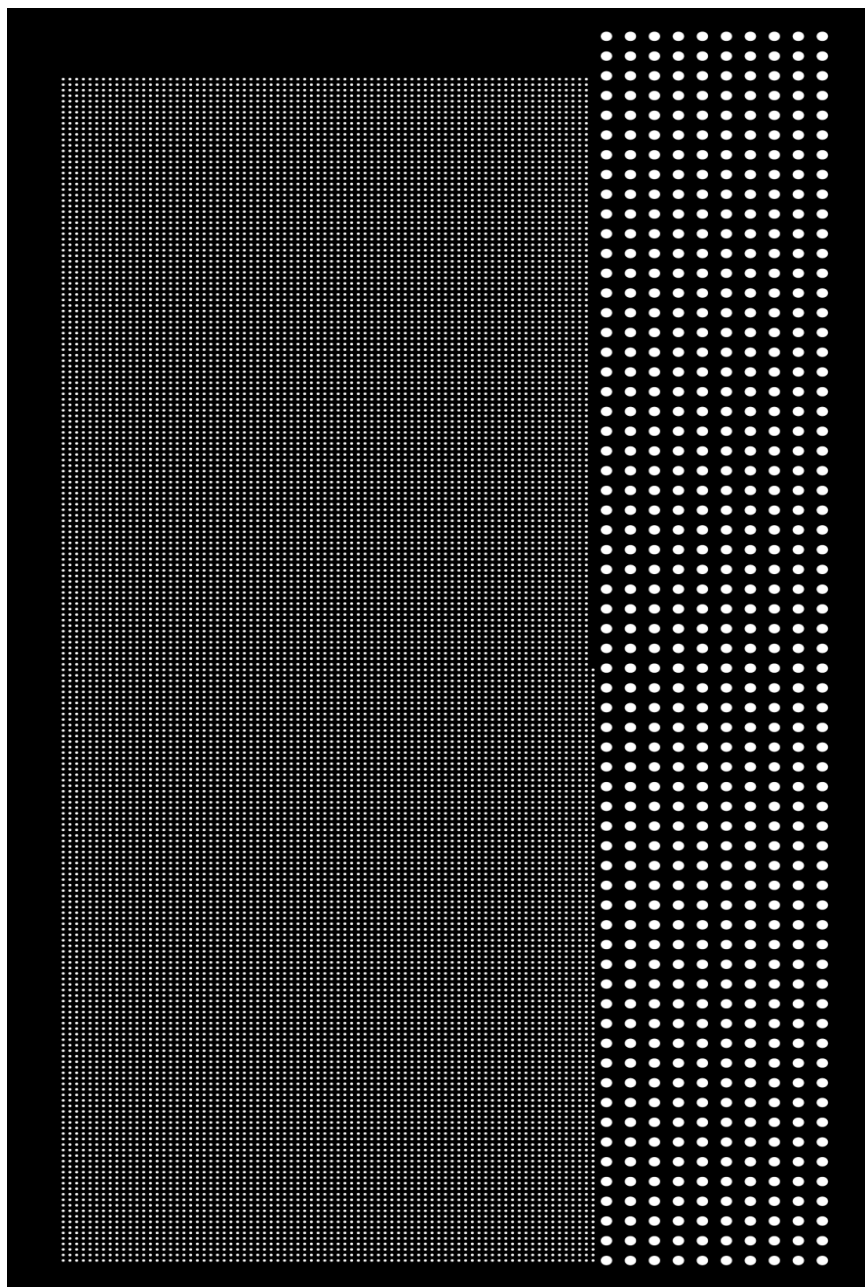


FIGURE 23 - IMAGE OF MODEL GEOMETRY

Appendix C – Nanoparticle Size Data

TABLE 1 - EXCEL DATA SUMMARY OF NANOPARTICLE SIZES

Particle	Quoted Size (nm)	Average Size (nm)	Deviation (nm)	Combined Average	Combined Deviation
Al ₂ O ₃	135	182.4202	48.72769	182.4202	48.72769
Al ₂ O ₃	135				
BaTiO ₃	100	123.6181	24.8146	117.736	23.109005
BaTiO ₃	100	111.8539	21.40341		
CeO ₂	10--30	20.565	8.83977	20.565	8.83977
CeO ₂	10--30				
WO ₃	60	47.90318	11.16033	47.90318	11.16033
WO ₃	60				
ZrO ₂	40	43.94879	12.77819	48.772985	14.71234
ZrO ₂	40	53.59718	16.64649		
SiC	45--65	64.64333333	14.30409848	56.90147799	13.17322751
SiC	45--65	49.15962264	12.04235653		
ZnO	10--30	41.7986	14.40170726	41.7986	14.40170726
ZnO	10--30				
TiO ₂	10--25	46.7484	15.09787526	46.7484	15.09787526
TiO ₂	10--25				
MgO	40	147.377	45.68191427	147.377	45.68191427
MgO	40				

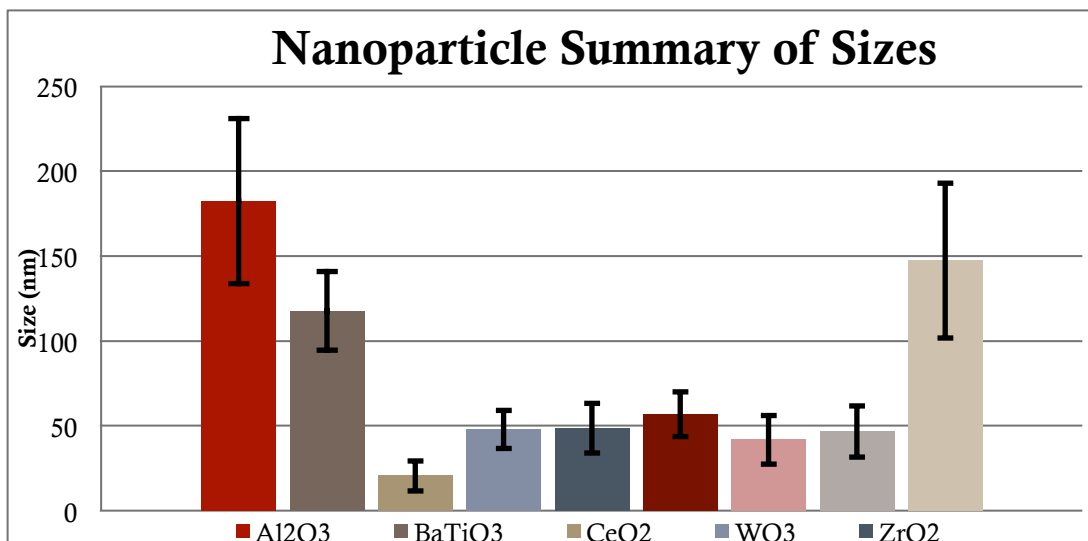


FIGURE 24 - NANO PARTICLE SUMMARY OF SIZES

Appendix D – X-Ray Diffraction Data

TABLE 2 – EXCEL DATA SUMMARY OF FWHM FROM XRD ANALYSIS

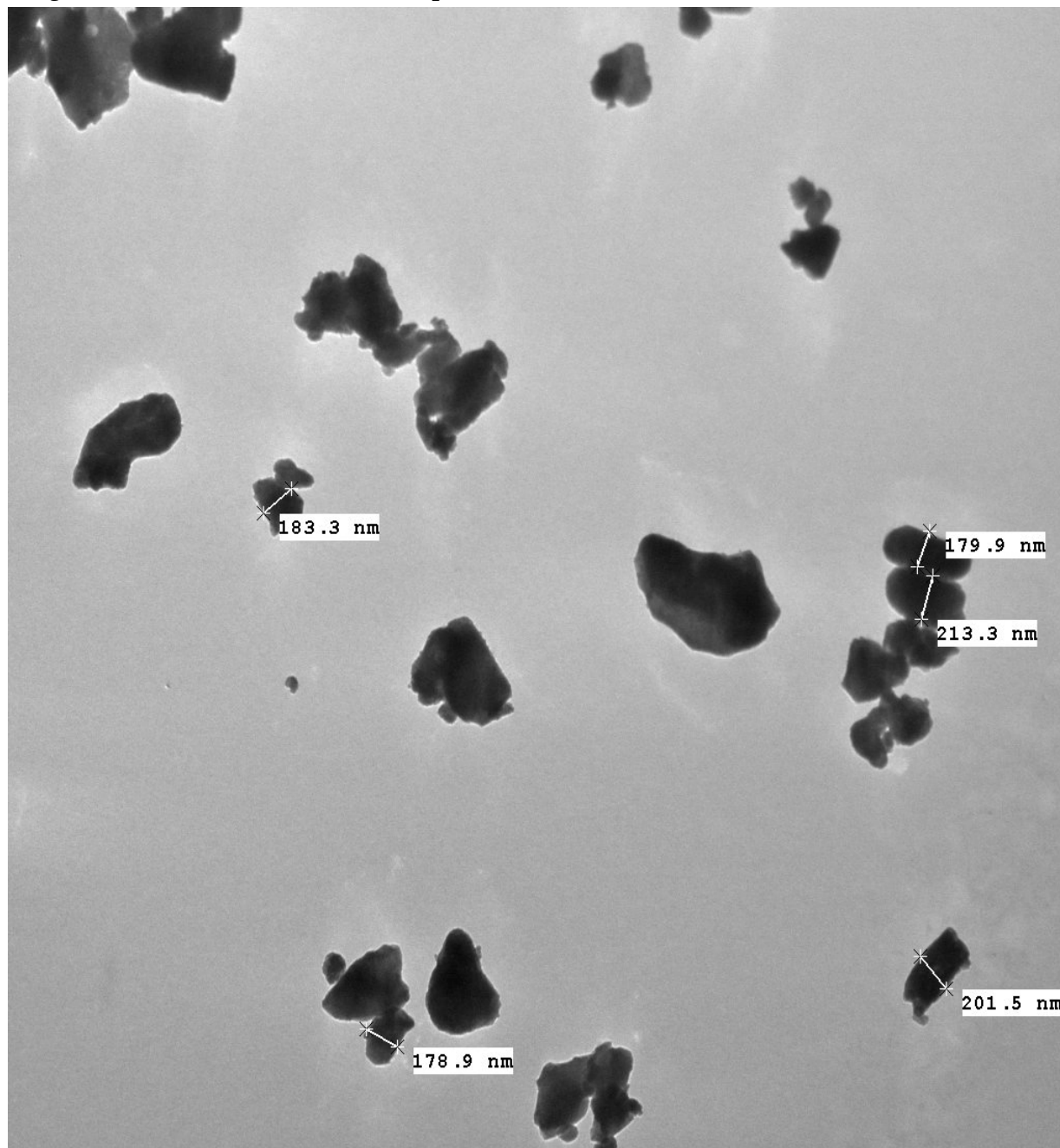
FWHM DATA		Undoped Cermet ZnO peak	Undoped MOCVD ZnO peak	
		576.00	763.20	
12 Hour Data Set				
ZnO 1250-10 peak	ZnO 1250-20 peak	ZnO 1250-30 peak	ZnO 1250-40 peak	ZnO 1250-50 peak
640.80	597.60	576.00	633.60	586.80
ZnO 1255-10 peak	ZnO 1255-20 peak	ZnO 1255-30 peak	ZnO 1255-40 peak	ZnO 1255-50 peak
554.40	579.60	676.80	597.60	525.60
ZnO 1260-10 peak	ZnO 1260-20 peak	ZnO 1260-30 peak	ZnO 1260-40 peak	ZnO 1260-50 peak
619.20	597.60	586.80	576.00	568.80
ZnO 1265-10 peak	ZnO 1265-20 peak	ZnO 1265-30 peak	ZnO 1265-40 peak	ZnO 1265-50 peak
547.20	651.60	576.00	597.60	597.60
ZnO 1270-10 peak	ZnO 1270-20 peak	ZnO 1270-30 peak	ZnO 1270-40 peak	ZnO 1270-50 peak
680.40	640.80	666.00	604.80	680.40
ZnO 1275-10 peak	ZnO 1275-20 peak	ZnO 1275-30 peak	ZnO 1275-40 peak	ZnO 1275-50 peak
680.40	619.20	644.40	637.20	554.40
ZnO 1280-10 peak	ZnO 1280-20 peak	ZnO 1280-30 peak	ZnO 1280-40 peak	ZnO 1280-50 peak
536.40	601.20	576.00	619.20	576.00
ZnO 1285-10 peak	ZnO 1285-20 peak	ZnO 1285-30 peak	ZnO 1285-40 peak	ZnO 1285-50 peak
568.80	615.60	676.80	561.60	536.40
ZnO 1290-10 peak	ZnO 1290-20 peak	ZnO 1290-30 peak	ZnO 1290-40 peak	ZnO 1290-50 peak
550.80	576.00	698.40	597.60	658.80
ZnO 1295-10 peak	ZnO 1295-20 peak	ZnO 1295-30 peak	ZnO 1295-40 peak	ZnO 1295-50 peak
601.20	658.80	576.00	586.80	694.80
24 Hour Data Set				
ZnO 2450-10 peak	ZnO 2450-20 peak	ZnO 2450-30 peak	ZnO 2450-40 peak	ZnO 2450-50 peak

586.80	698.40	597.60	547.20	676.80
ZnO 2455-10 peak	ZnO 2455-20 peak	ZnO 2455-30 peak	ZnO 2455-40 peak	ZnO 2455-50 peak
687.60	637.20	838.80	655.20	554.40
ZnO 2460-10 peak	ZnO 2460-20 peak	ZnO 2460-30 peak	ZnO 2460-40 peak	ZnO 2460-50 peak
594.00	586.80	619.20	576.00	565.20
ZnO 2465-10 peak	ZnO 2465-20 peak	ZnO 2465-30 peak	ZnO 2465-40 peak	ZnO 2465-50 peak
626.40	655.20	1130.40	662.40	586.80
ZnO 2470-10 peak	ZnO 2470-20 peak	ZnO 2470-30 peak	ZnO 2470-40 peak	ZnO 2470-50 peak
615.60	558.00	637.20	536.40	514.80
ZnO 2475-10 peak	ZnO 2475-20 peak	ZnO 2475-30 peak	ZnO 2475-40 peak	ZnO 2475-50 peak
619.20	597.60	673.20	637.20	669.60
ZnO 2480-10 peak	ZnO 2480-20 peak	ZnO 2480-30 peak	ZnO 2480-40 peak	ZnO 2480-50 peak
608.40	615.60	554.40	547.20	676.80
ZnO 2485-10 peak	ZnO 2485-20 peak	ZnO 2485-30 peak	ZnO 2485-40 peak	ZnO 2485-50 peak
658.80	608.40	651.60	597.60	558.00
ZnO 2490-10 peak	ZnO 2490-20 peak	ZnO 2490-30 peak	ZnO 2490-40 peak	ZnO 2490-50 peak
608.40	637.20	658.80	558.00	547.20
ZnO 2495-10 peak	ZnO 2495-20 peak	ZnO 2495-30 peak	ZnO 2495-40 peak	ZnO 2495-50 peak
597.60	676.80	608.40	536.40	554.40
36 Hour Data Set				
ZnO 3650-10 peak	ZnO 3650-20 peak	ZnO 3650-30 peak	ZnO 3650-40 peak	ZnO 3650-50 peak
648.00	550.80	604.80	554.40	586.80
ZnO 3655-10 peak	ZnO 3655-20 peak	ZnO 3655-30 peak	ZnO 3655-40 peak	ZnO 3655-50 peak
633.60	658.80	658.80	561.60	637.20
ZnO 3660-10 peak	ZnO 3660-20 peak	ZnO 3660-30 peak	ZnO 3660-40 peak	ZnO 3660-50 peak
630.00	536.40	547.20	543.60	597.60
ZnO 3665-10 peak	ZnO 3665-20 peak	ZnO 3665-30 peak	ZnO 3665-40 peak	ZnO 3665-50 peak
550.80	597.60	547.20	637.20	637.20
ZnO 3670-10 peak	ZnO 3670-20 peak	ZnO 3670-30 peak	ZnO 3670-40 peak	ZnO 3670-50 peak
568.80	594.00	619.20	597.60	576.00
ZnO 3675-10 peak	ZnO 3675-20 peak	ZnO 3675-30 peak	ZnO 3675-40 peak	ZnO 3675-50 peak
781.20	658.80	586.80	594.00	597.60

ZnO 3680-10 peak	ZnO 3680-20 peak	ZnO 3680-30 peak	ZnO 3680-40 peak	ZnO 3680-50 peak
565.20	669.60	622.80	547.20	594.00
ZnO 3685-10 peak	ZnO 3685-20 peak	ZnO 3685-30 peak	ZnO 3685-40 peak	ZnO 3685-50 peak
608.40	619.20	576.00	637.20	597.60
ZnO 3690-10 peak	ZnO 3690-20 peak	ZnO 3690-30 peak	ZnO 3690-40 peak	ZnO 3690-50 peak
694.80	644.40	615.60	576.00	576.00
ZnO 3695-10 peak	ZnO 3695-20 peak	ZnO 3695-30 peak	ZnO 3695-40 peak	ZnO 3695-50 peak
597.60	626.40	597.60	576.00	615.60

Appendix E – TEM Measurements on Nanoparticles - Images

Images of TEM Measurements on Nanoparticles



Sample 2H 001 AL203.tif

AL203

Print Mag: 32900x @ 7.0 in

9:21:32 AM 7/18/2012

Microscopist: ALT

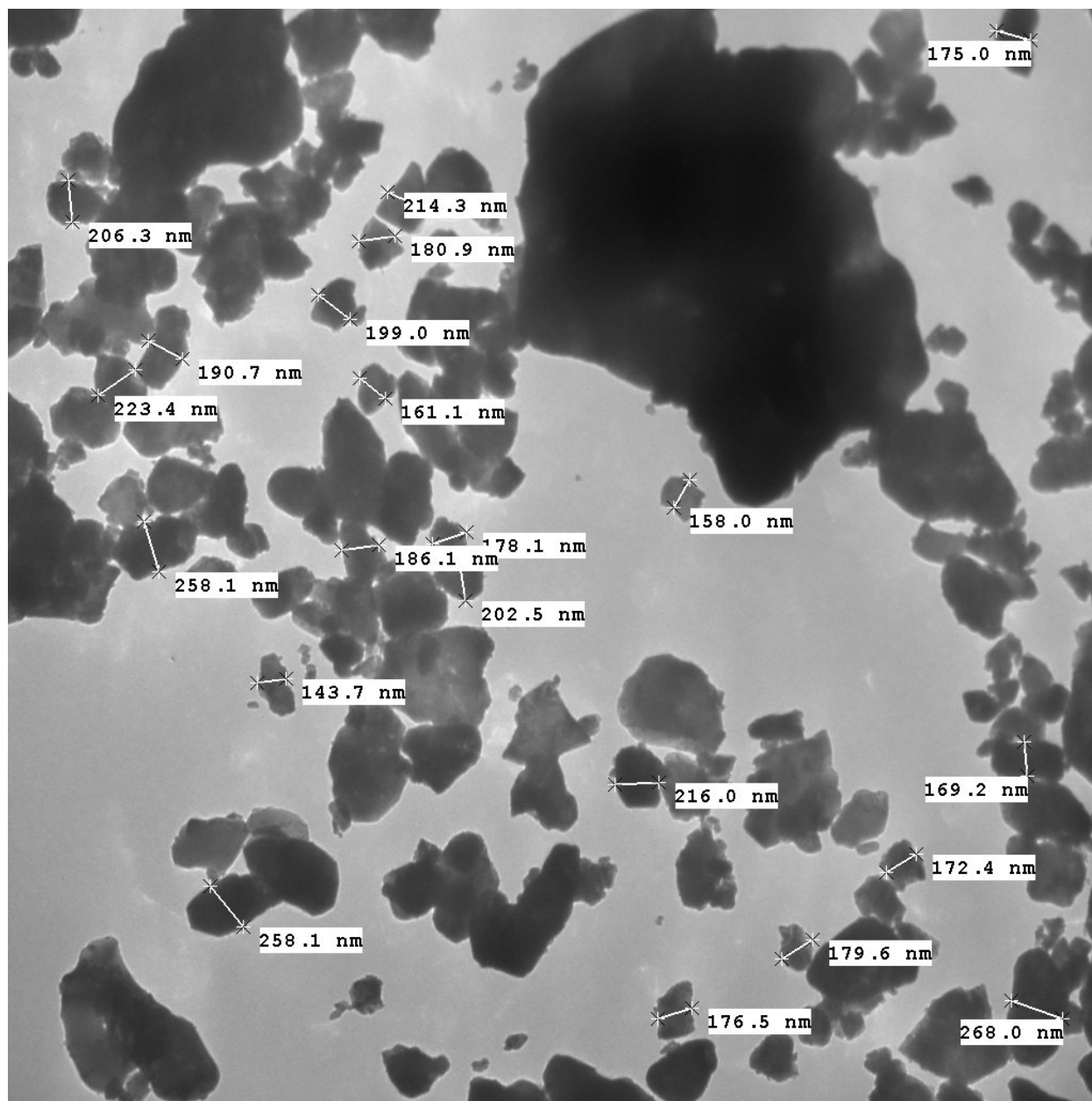
500 nm

HV=80.0kV

Direct Mag: 19000x

AMT Camera System

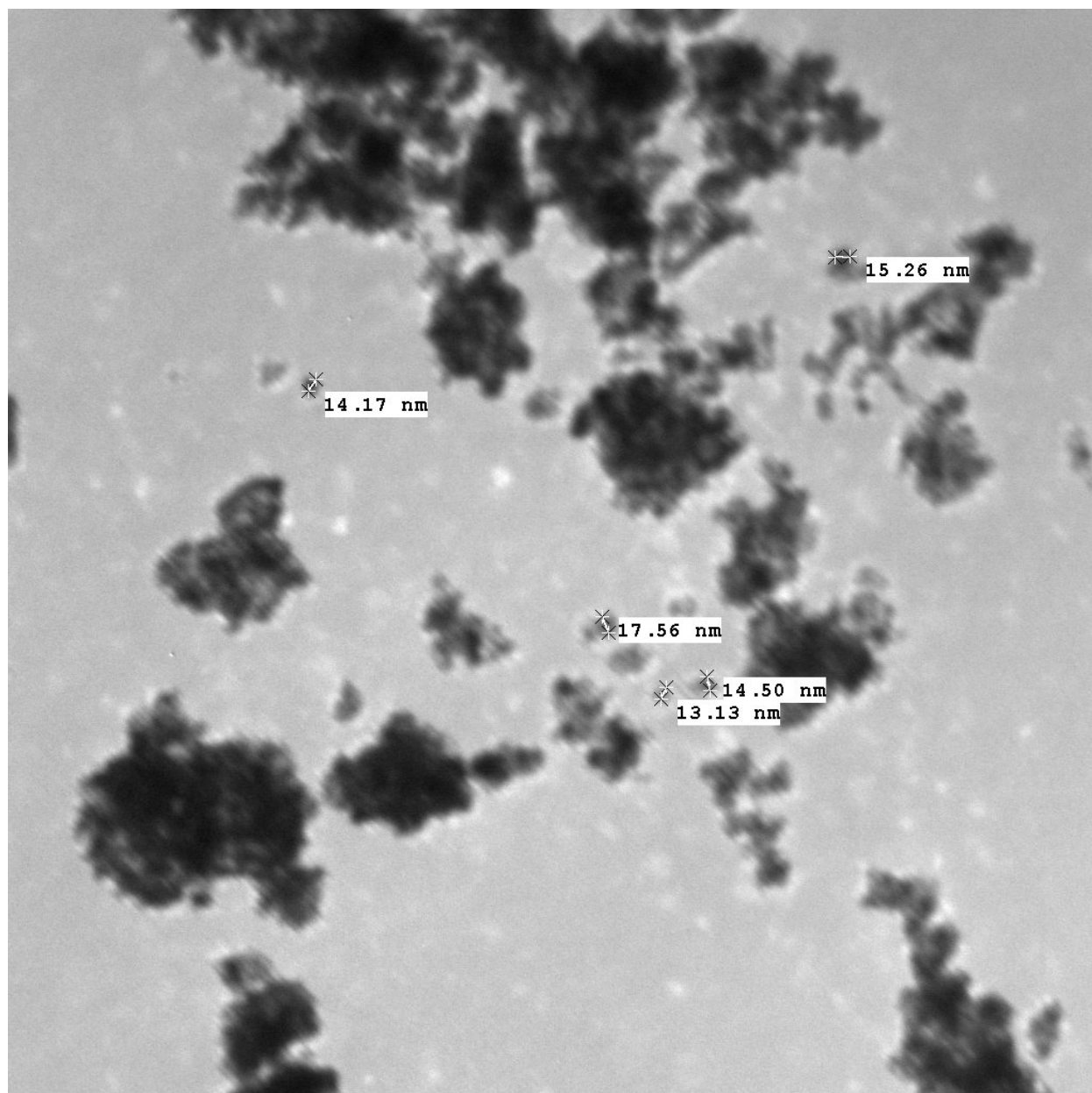
FIGURE 25 - TEM MEASUREMENTS – SAMPLE 2H 001 AL203.TIF



Sample 2H 003 Al2O3.tif
 Al2O3
 Print Mag: 32900x @ 7.0 in
 9:42:45 AM 7/18/2012
 Microscopist: ALT

500 nm
 HV=80.0kV
 Direct Mag: 19000x
 AMT Camera System

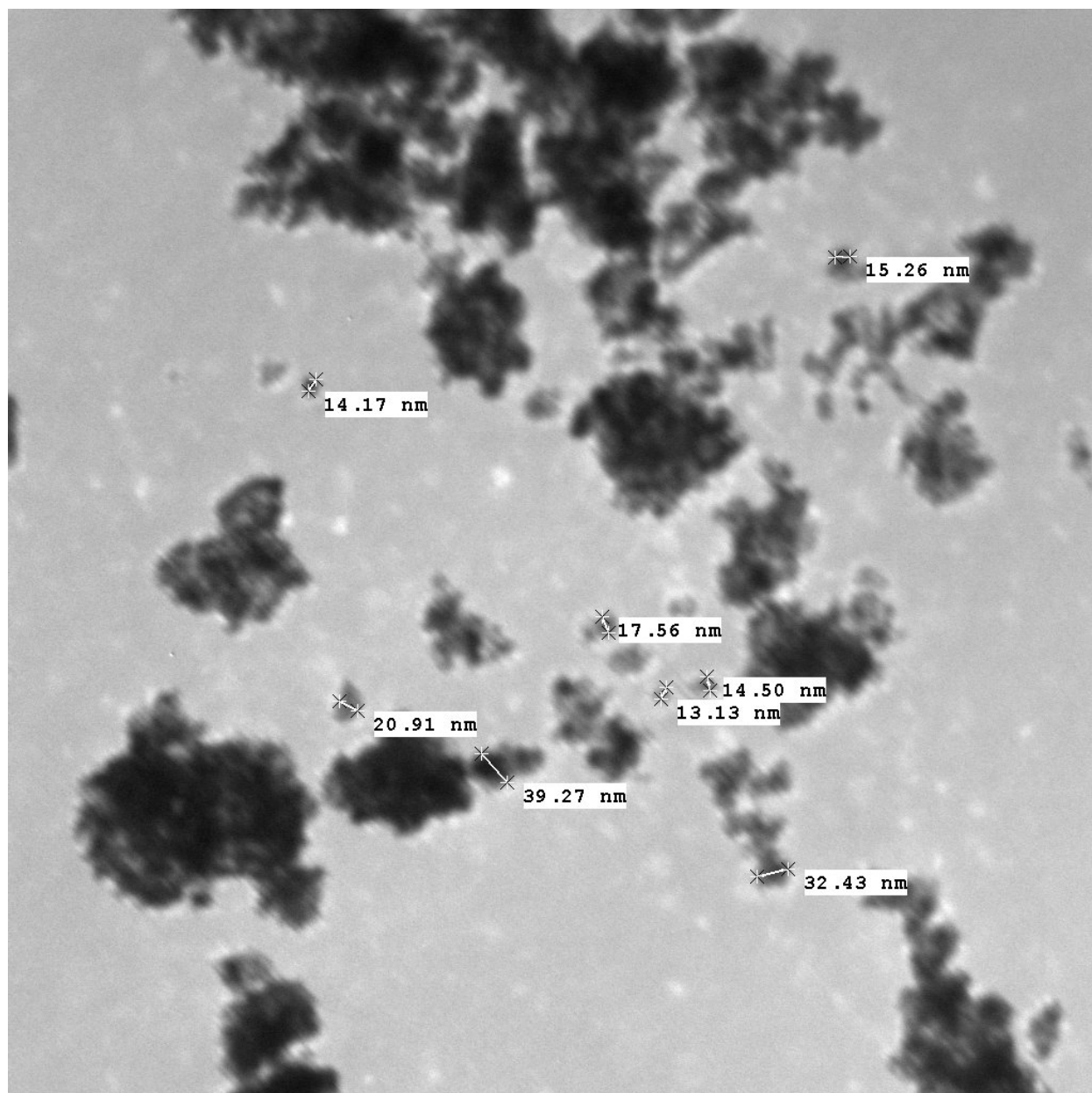
FIGURE 26 - TEM MEASUREMENTS – SAMPLE 2H 003 AL2O3.TIF



Sample 2J 002 CeO2.tif
 CeO2
 Print Mag: 160000x @ 7.0 in
 12:00:53 PM 7/18/2012
 Microscopist: ALT

100 nm
 HV=80.0kV
 Direct Mag: 92000x
 AMT Camera System

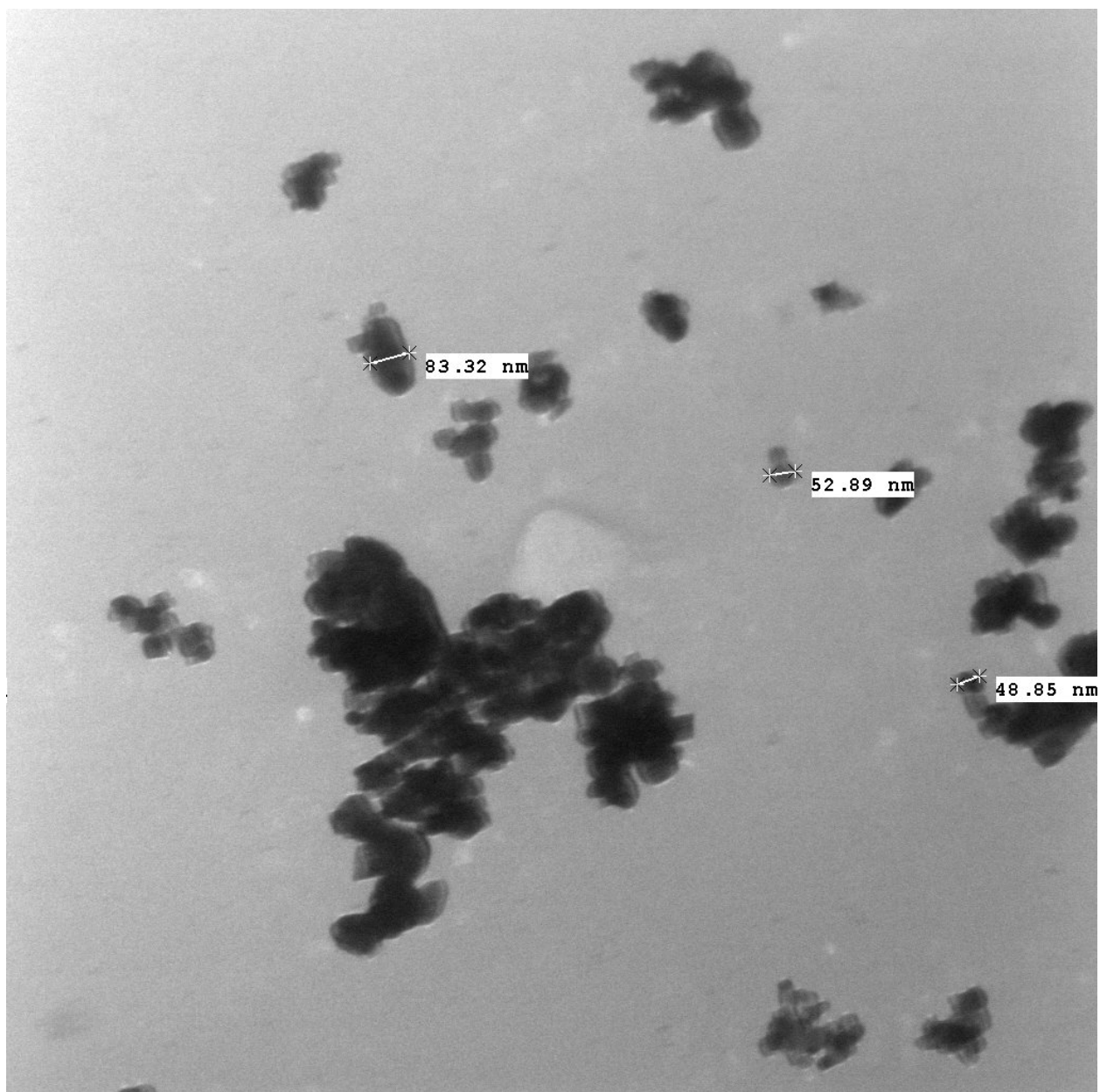
FIGURE 27 - TEM MEASUREMENTS – SAMPLE 2J 002 CE02.TIF



Sample 2J 003 CeO2.tif
 CeO2
 Print Mag: 160000x @ 7.0 in
 12:00:53 PM 7/18/2012
 Microscopist: ALT

100 nm
 HV=80.0kV
 Direct Mag: 92000x
 AMT Camera System

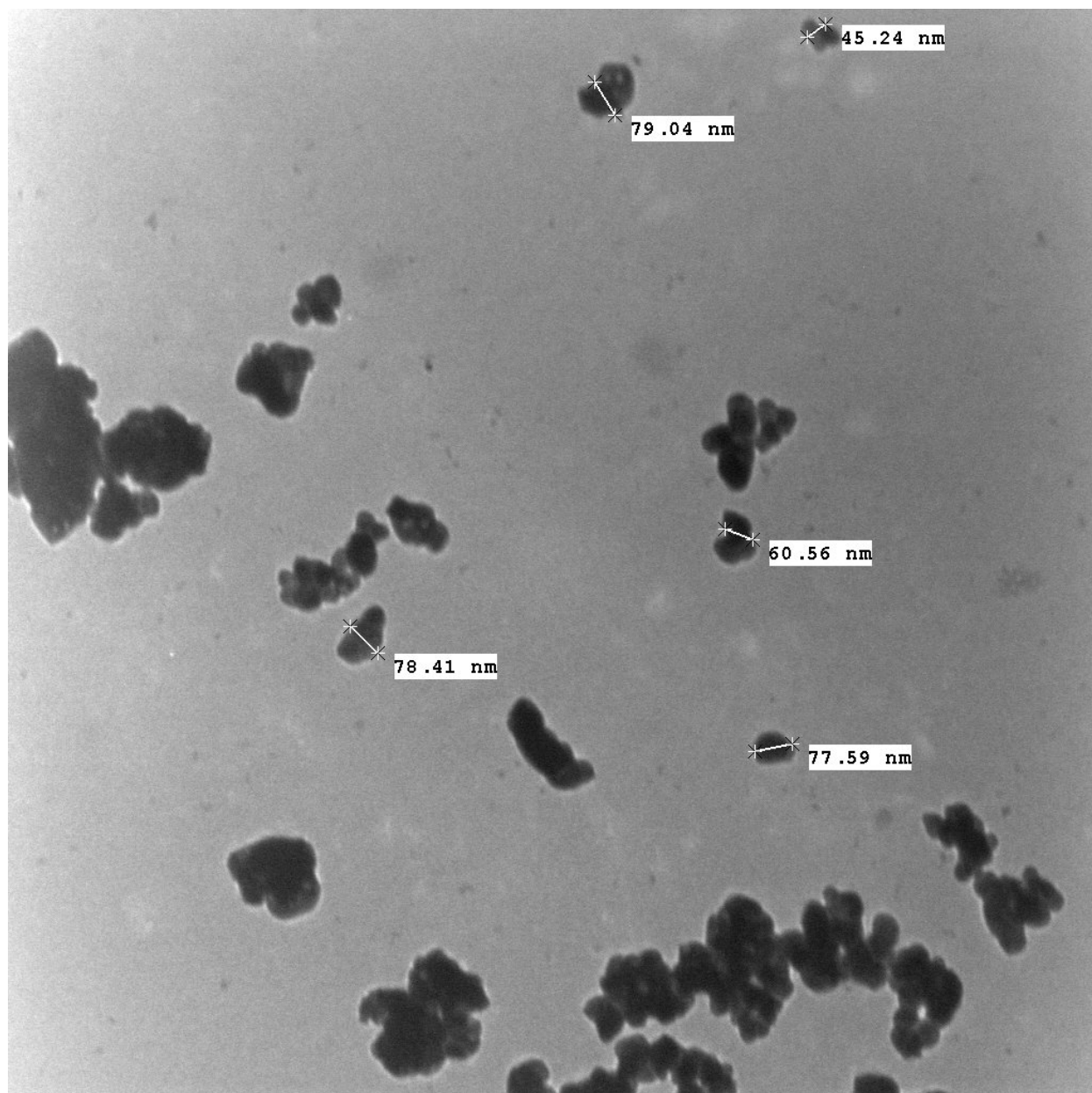
FIGURE 28 - TEM MEASUREMENTS – SAMPLE 2J 003 CE02.TIF



Sample 3C 001 ZrO2.tif
ZrO2
Print Mag: 79800x @ 7.0 in
3:40:22 PM 7/18/2012
Microscopist: ALT

500 nm
HV=80.0kV
Direct Mag: 46000x
AMT Camera System

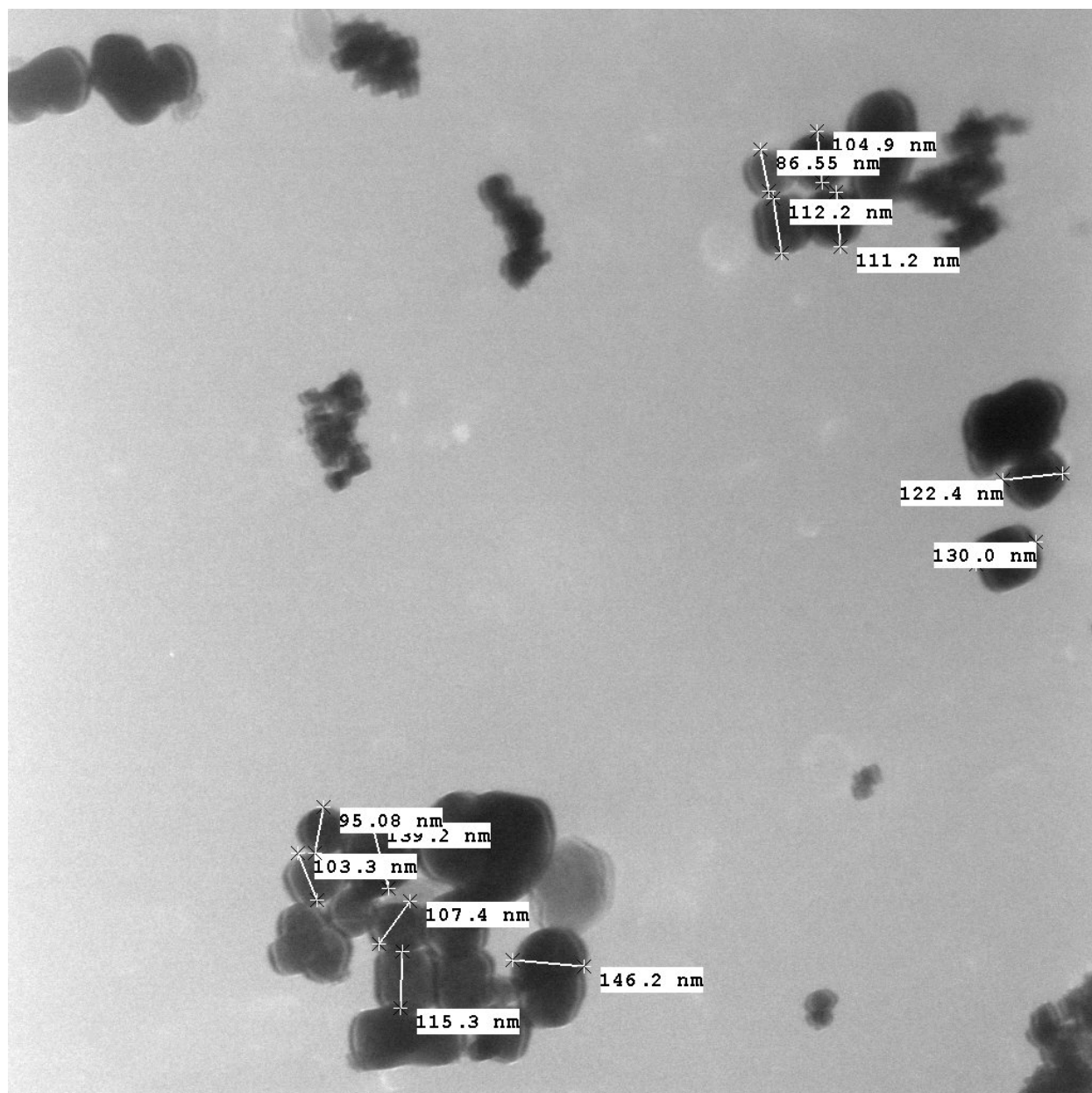
FIGURE 29 - TEM MEASUREMENTS – SAMPLE 3C 001 ZR02.TIF



Sample 3C 003 ZrO2.tif
ZrO2
Print Mag: 79800x @ 7.0 in
3:55:48 PM 7/18/2012
Microscopist: ALT

500 nm
HV=80.0kV
Direct Mag: 46000x
AMT Camera System

FIGURE 30 - TEM MEASUREMENTS – SAMPLE 3C 003 ZR02.TIF



Sample 2B 001 W03.tif

W03

Print Mag: 79800x @ 7.0 in

8:41:43 AM 7/20/2012

Microscopist: ALT

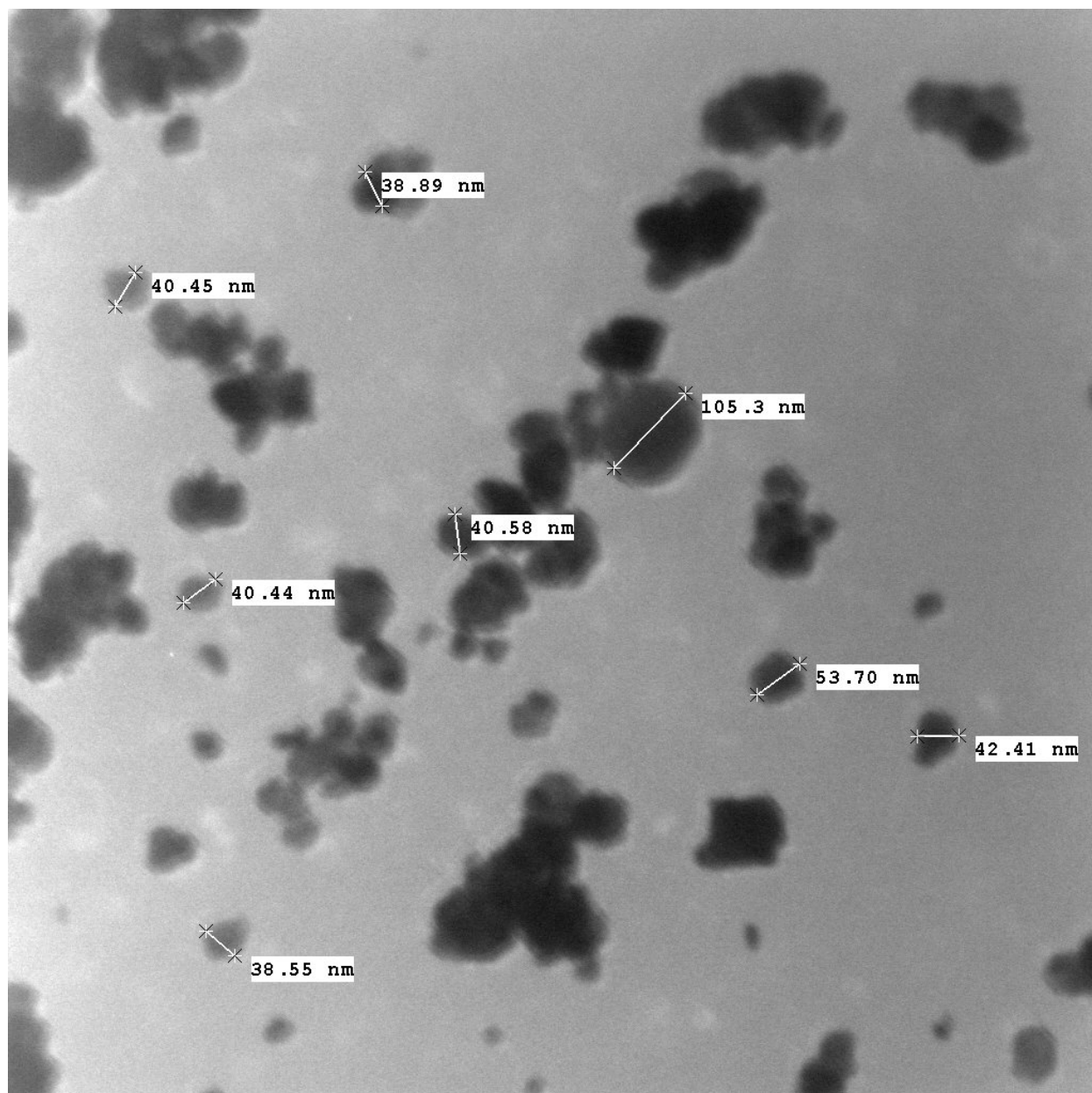
500 nm

HV=80.0kV

Direct Mag: 46000x

AMT Camera System

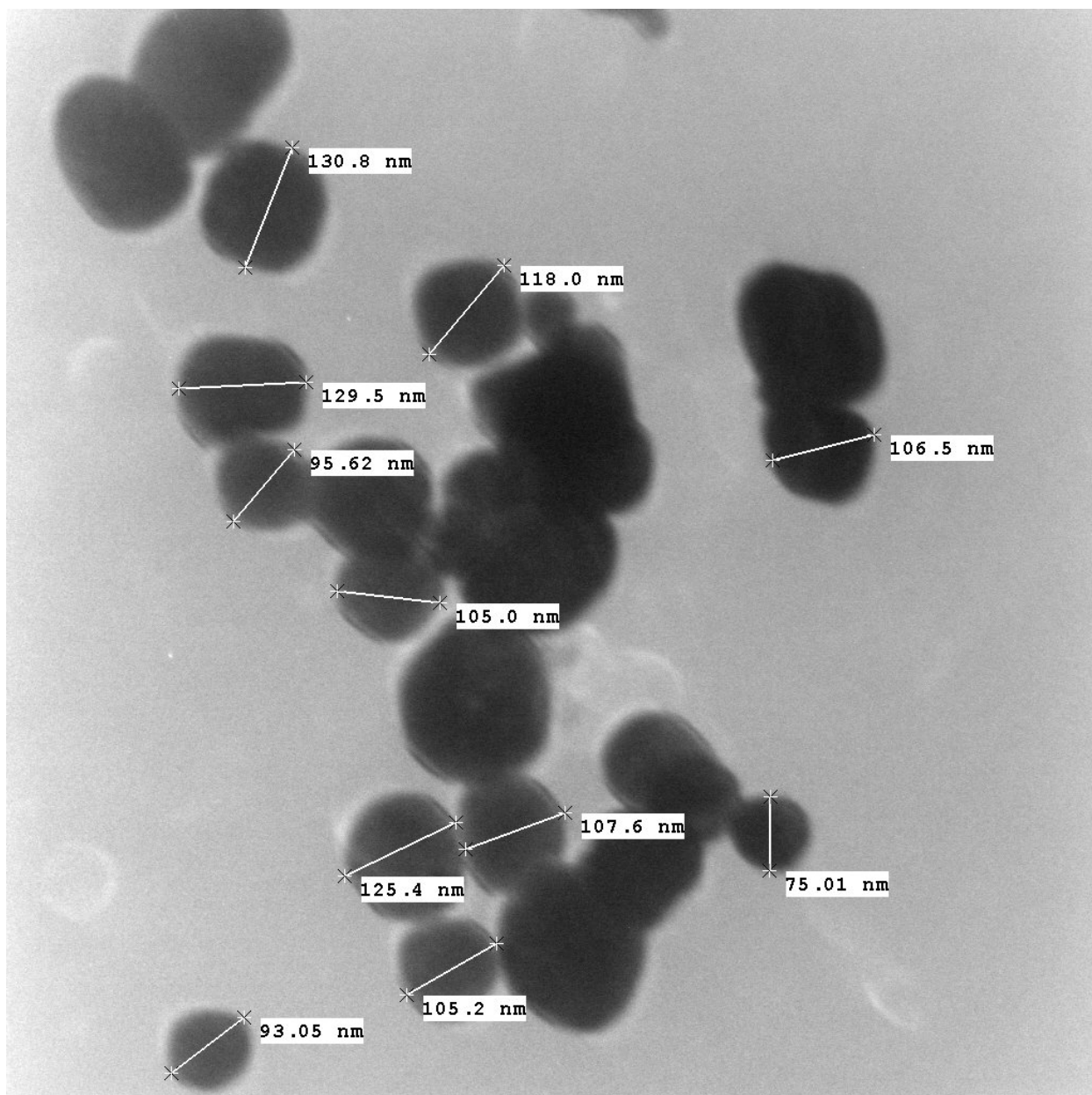
FIGURE 31 - TEM MEASUREMENTS – SAMPLE 2B 001 W03.TIF



Sample 2B 002 W03.tif
W03
Print Mag: 160000x @ 7.0 in
9:13:55 AM 7/20/2012
Microscopist: ALT

100 nm
HV=80.0kV
Direct Mag: 92000x
AMT Camera System

FIGURE 32 - TEM MEASUREMENTS – SAMPLE 2B 002 W03.TIF



Sample 1E 001 BaTiO3.tif
 BaTiO3
 Print Mag: 160000x @ 7.0 in
 1:23:51 PM 7/23/2012
 Microscopist: ALT

100 nm
 HV=80.0kV
 Direct Mag: 92000x
 AMT Camera System

FIGURE 33 - TEM MEASUREMENTS – SAMPLE 1E 001 BATiO3.TIF

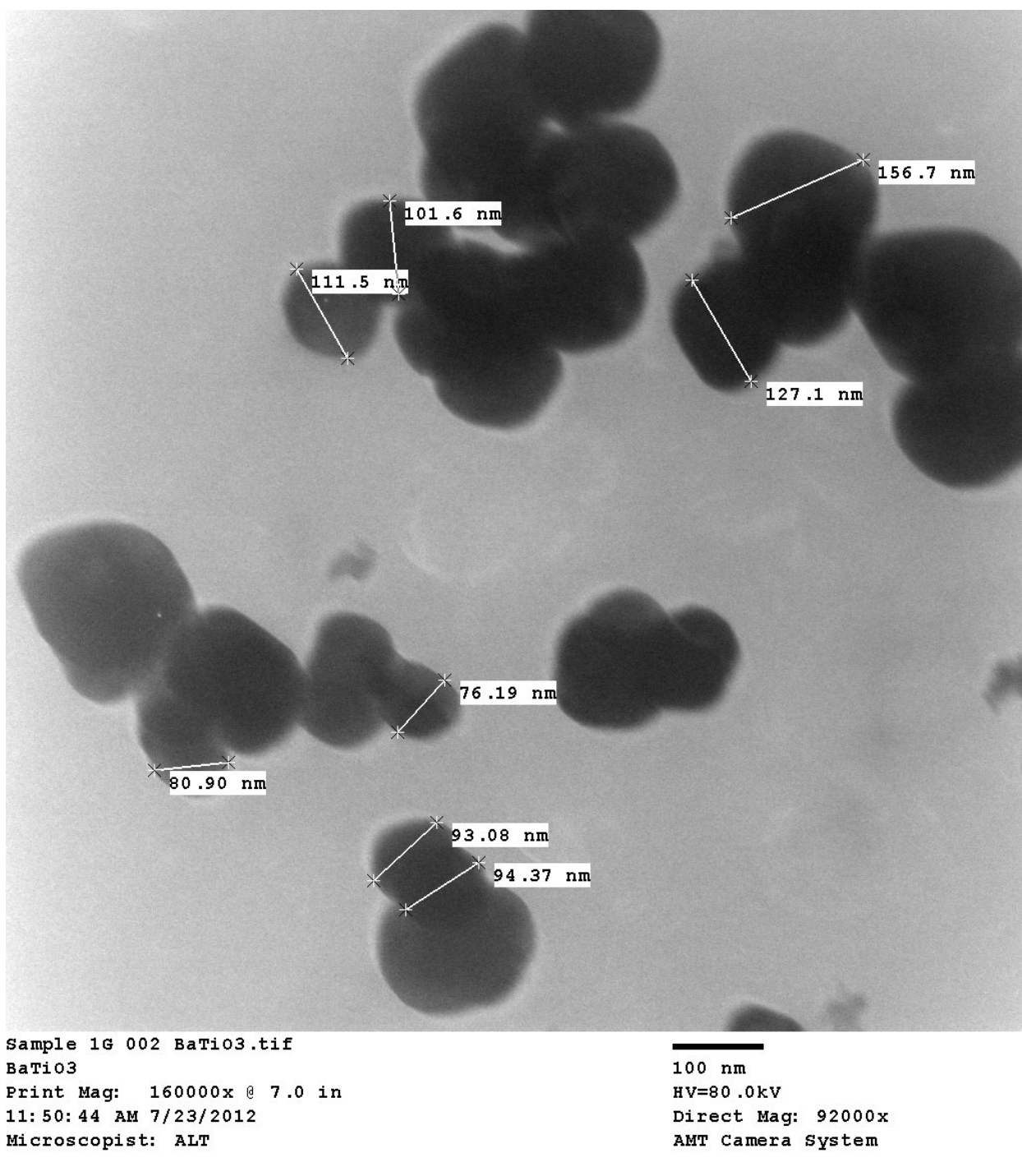
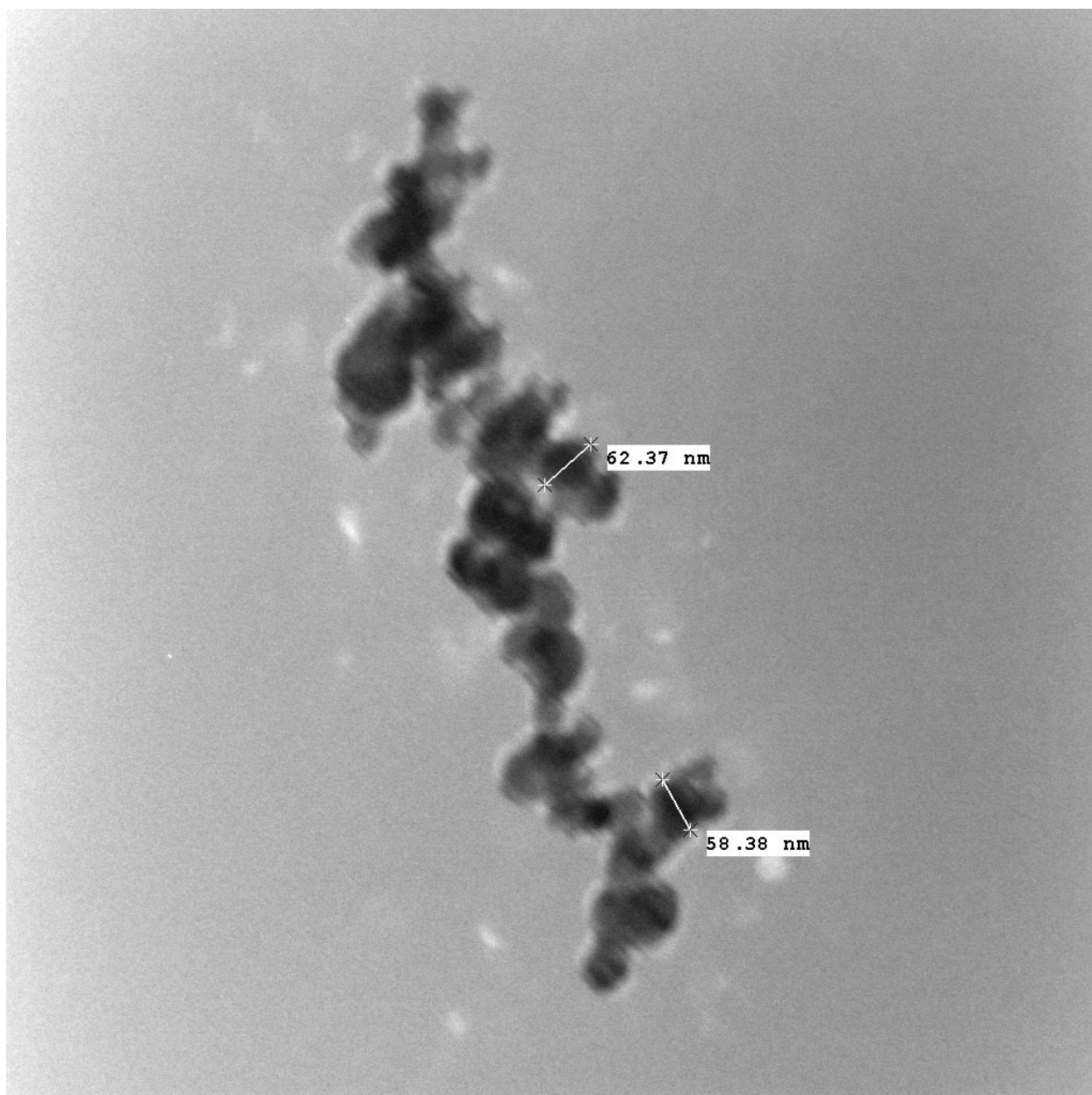


FIGURE 34 - TEM MEASUREMENTS – SAMPLE 1G 002 BATI03.TIF



Sample 4F 001 SiC.tif
SiC
Print Mag: 160000x @ 7.0 in
9:58:31 AM 7/27/2012
Microscopist: ALT

100 nm
HV=80.0kV
Direct Mag: 92000x
AMT Camera System

FIGURE 35 - TEM MEASUREMENTS – SAMPLE 4F 001 SiC.TIF

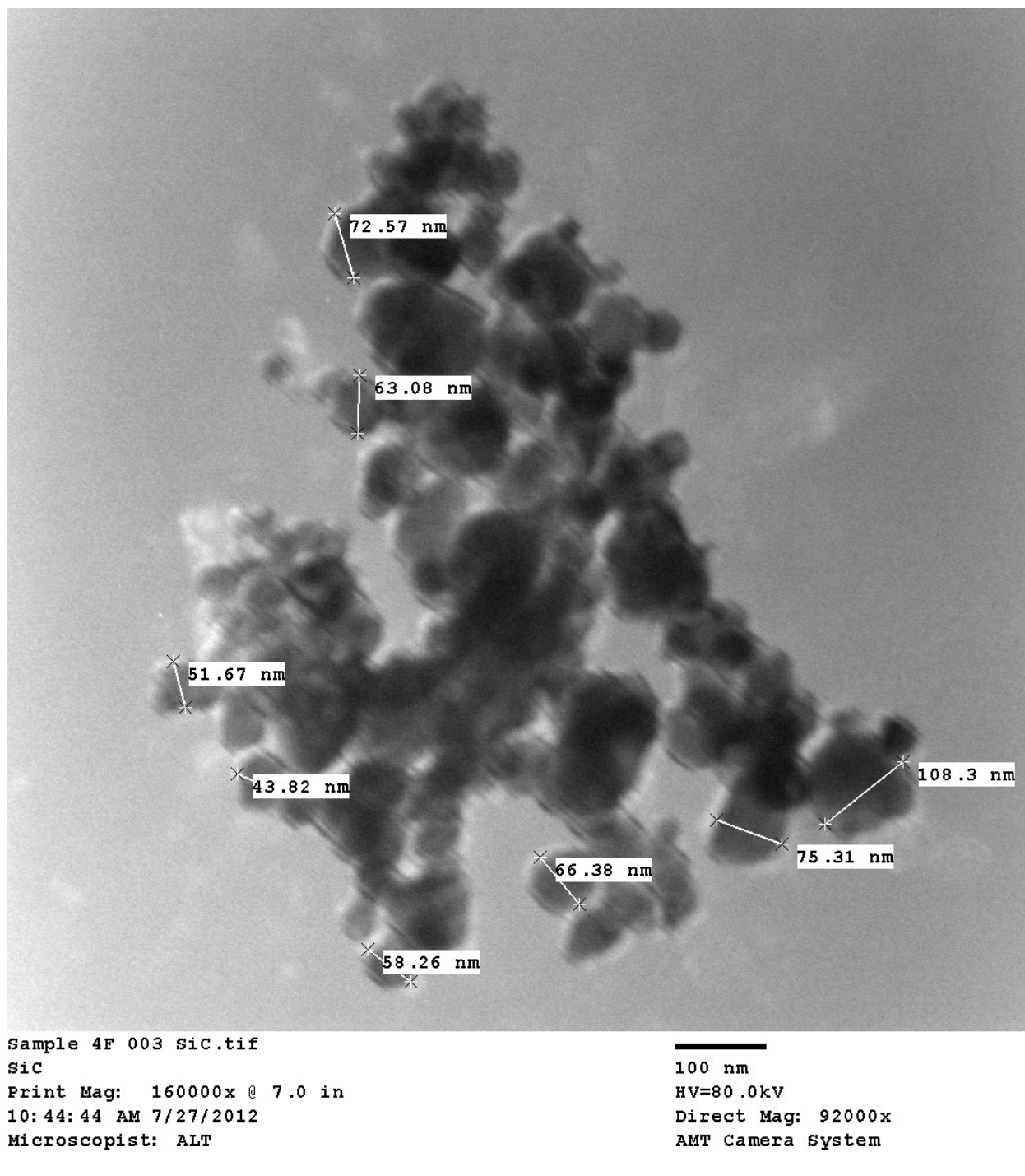
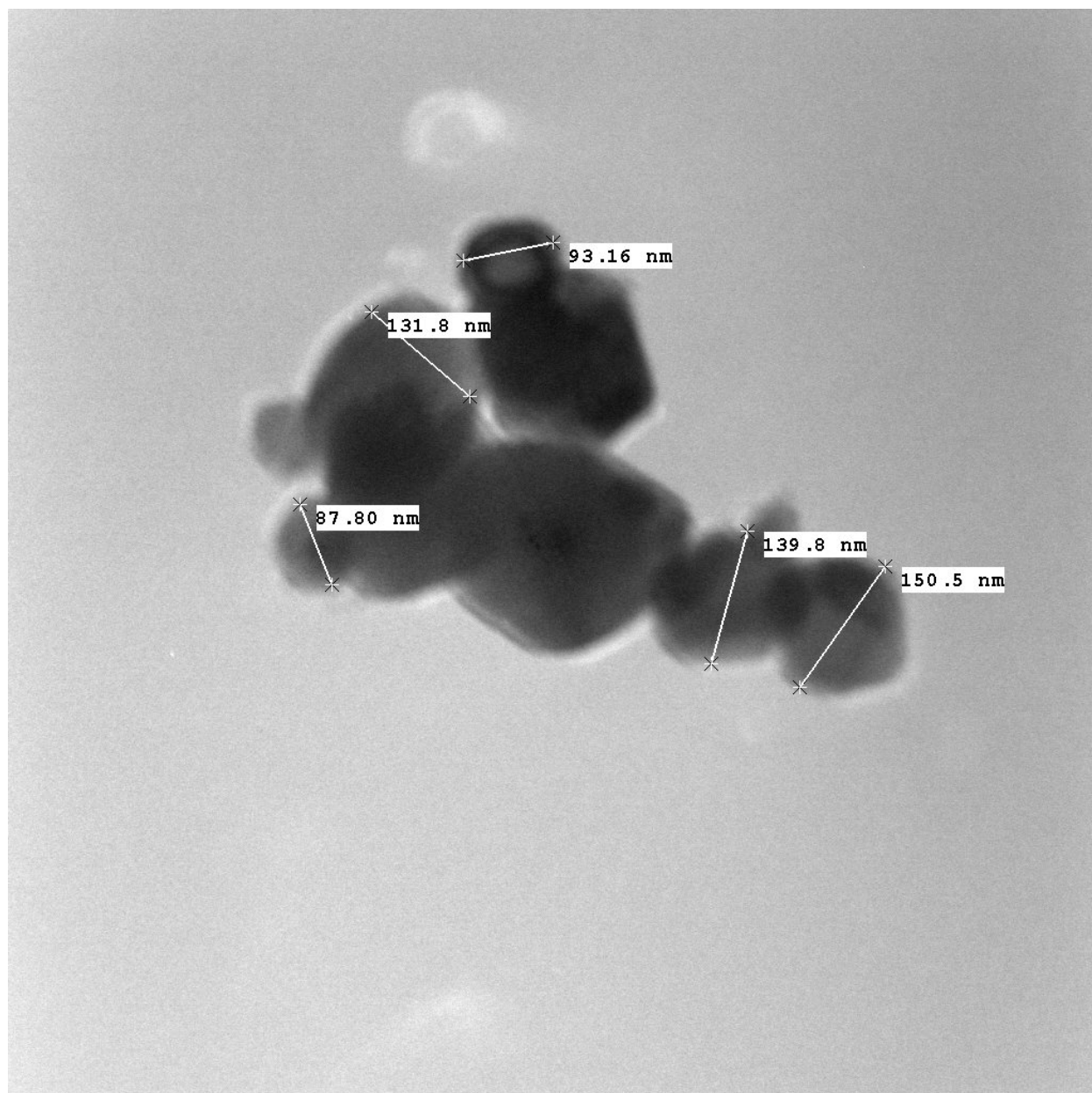


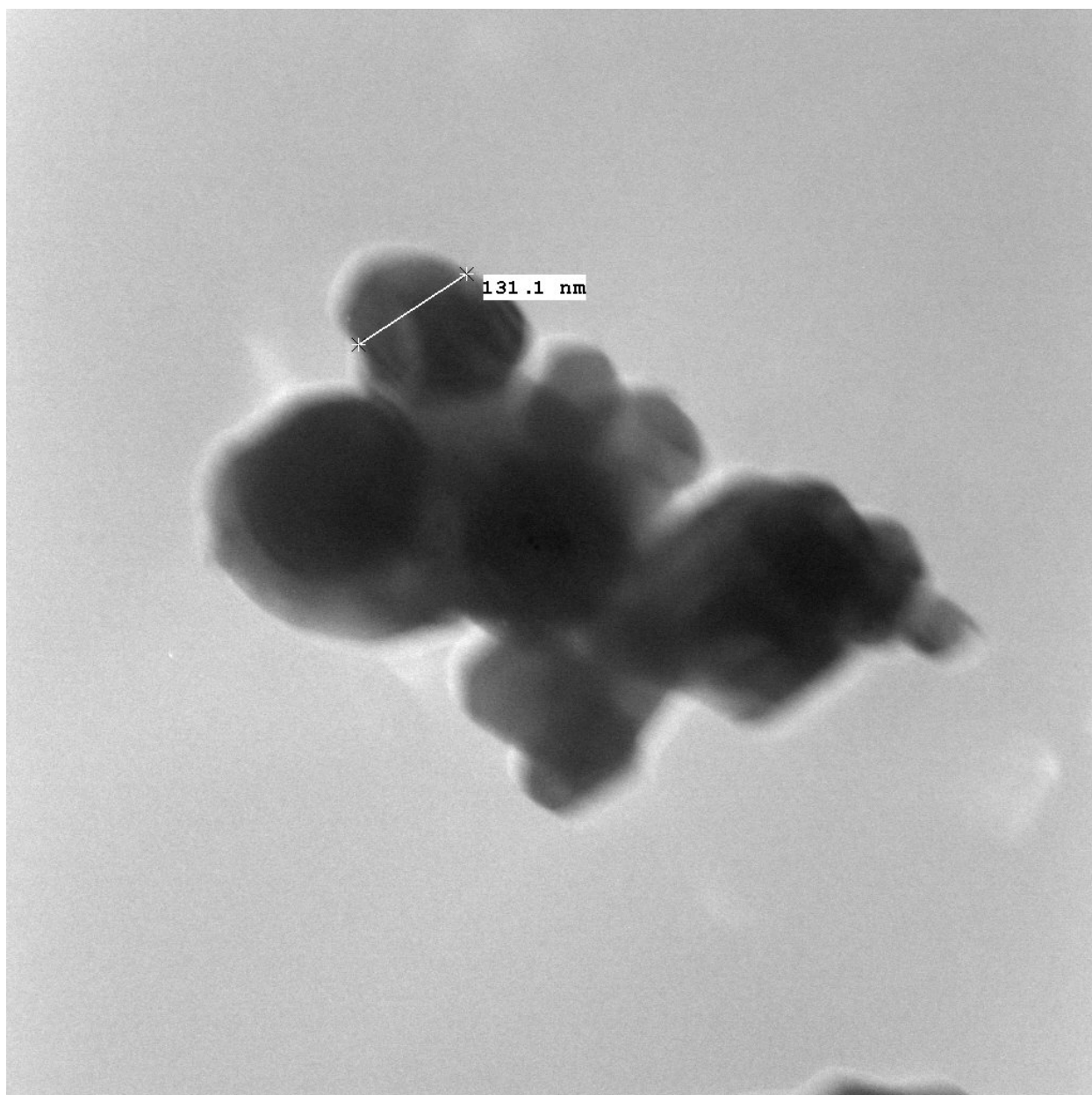
FIGURE 36 - TEM MEASUREMENTS – SAMPLE 4F 003 SiC.TIF



Sample 6F 001 MgO.tif
MgO
Print Mag: 160000x @ 7.0 in
3:14:00 PM 8/9/2012
Microscopist: ALT

100 nm
HV=80.0kV
Direct Mag: 92000x
AMT Camera System

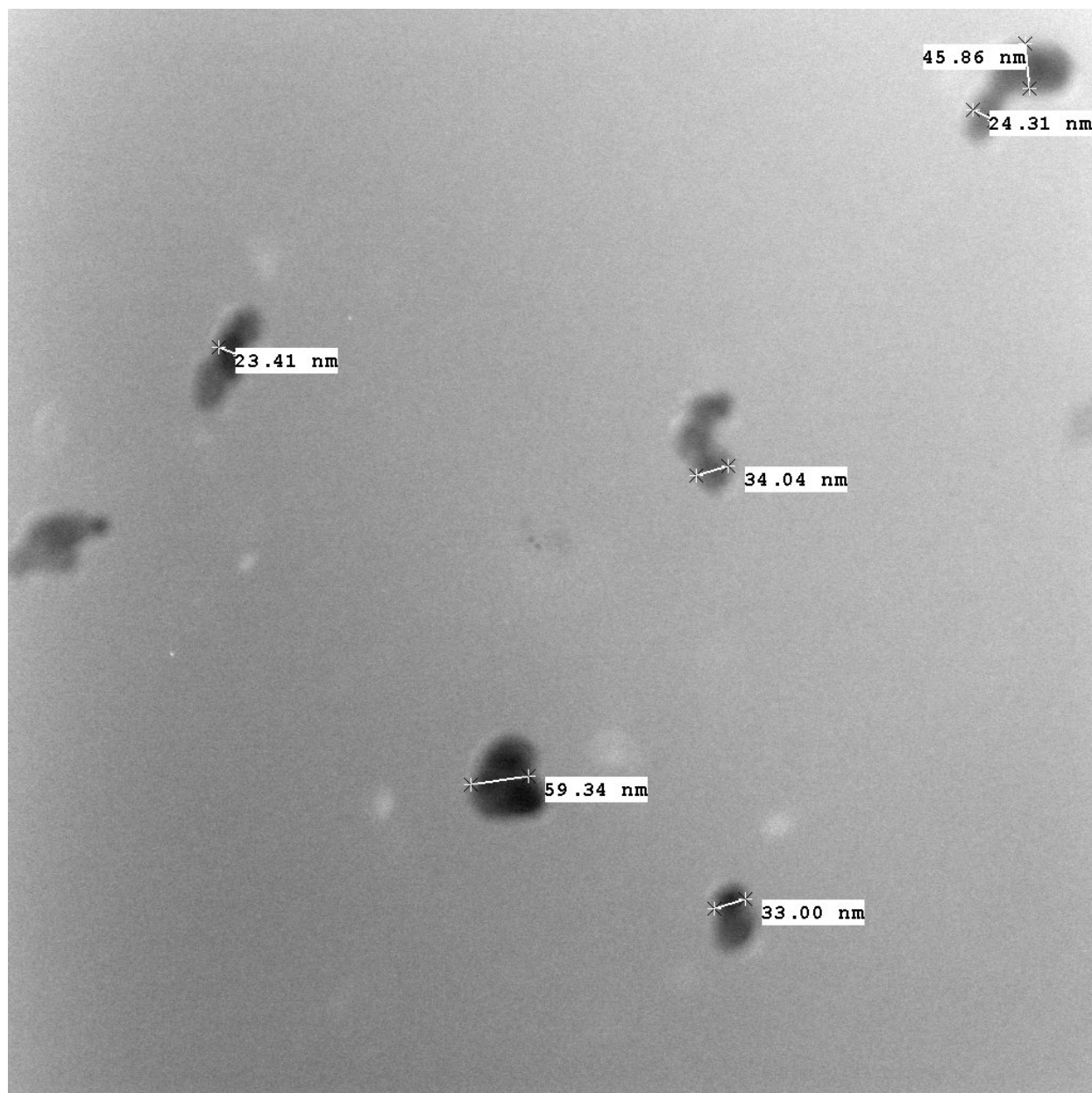
FIGURE 37 - TEM MEASUREMENTS – SAMPLE 6F 001 MGO.TIF



Sample 6F 006 MgO.tif
MgO
Print Mag: 160000x @ 7.0 in
3:53:01 PM 8/9/2012
Microscopist: ALT

100 nm
HV=80.0kV
Direct Mag: 92000x
AMT Camera System

FIGURE 38 - TEM MEASUREMENTS – SAMPLE 6F 006 MGO.TIF



Sample 6J 001 ZnO.tif
 ZnO
 Print Mag: 160000x @ 7.0 in
 9:32:58 AM 8/10/2012
 Microscopist: ALT

100 nm
 HV=80.0kV
 Direct Mag: 92000x
 AMT Camera System

FIGURE 39 - TEM MEASUREMENTS – SAMPLE 6J 001 ZNO.TIF

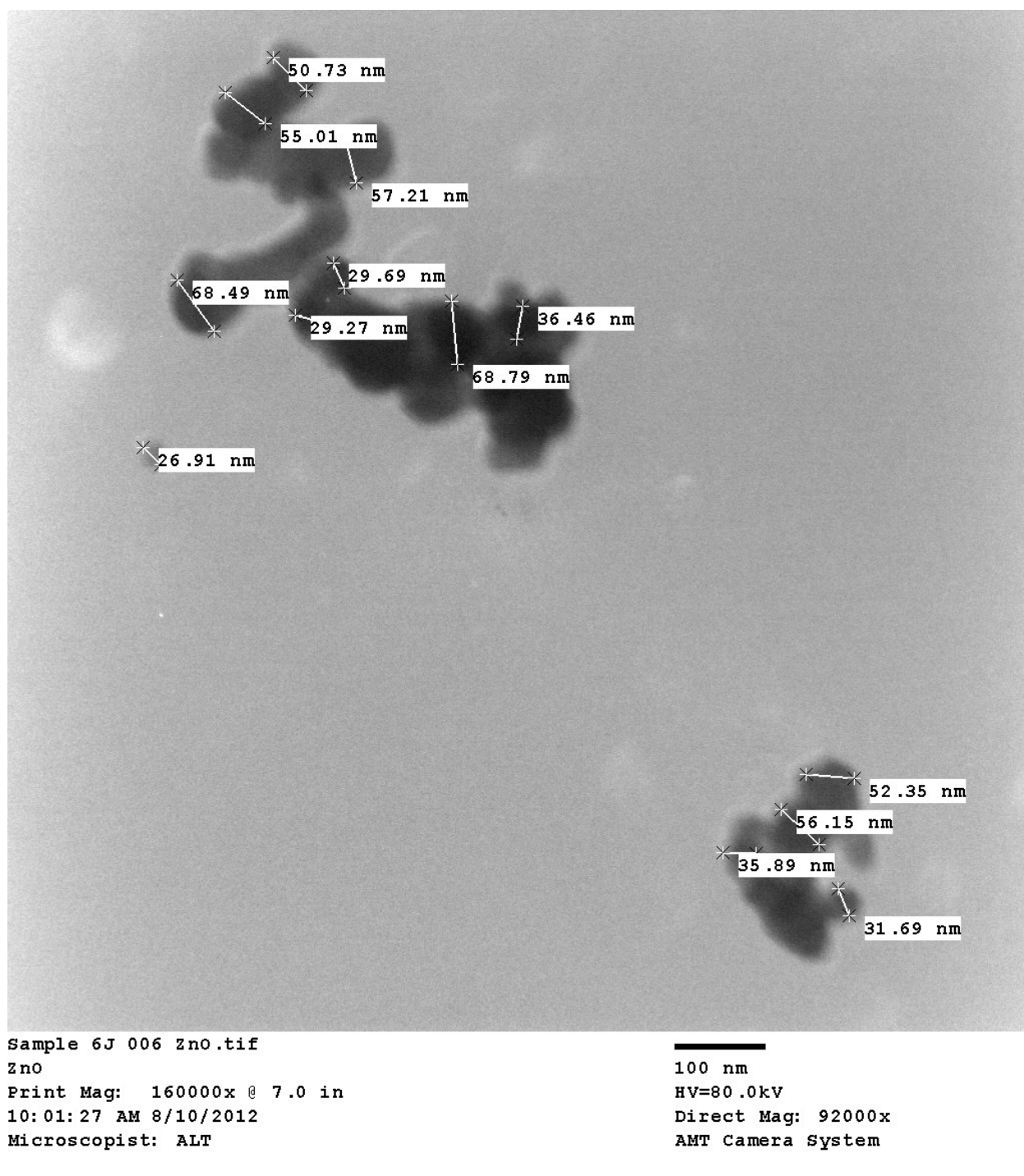
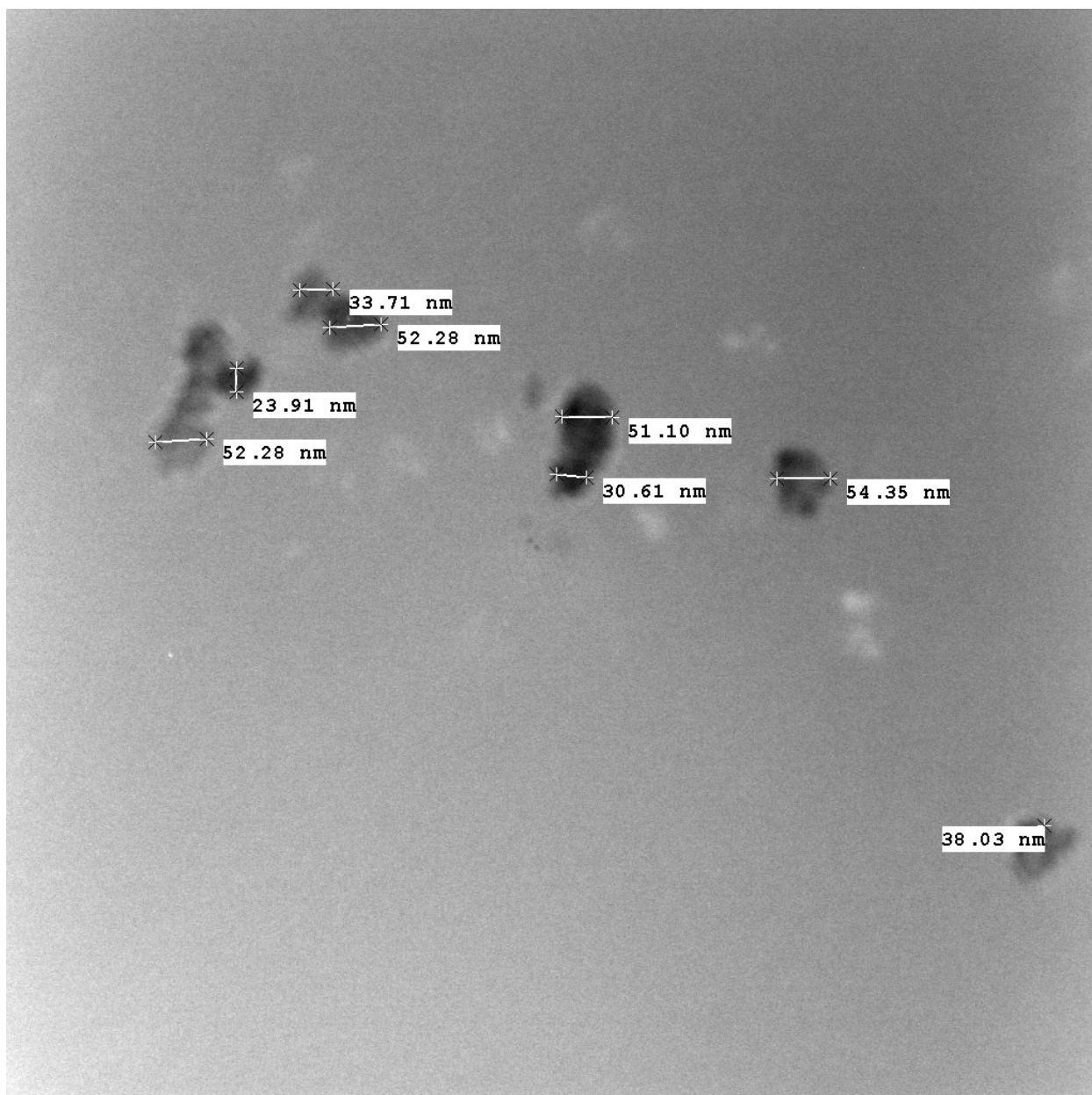


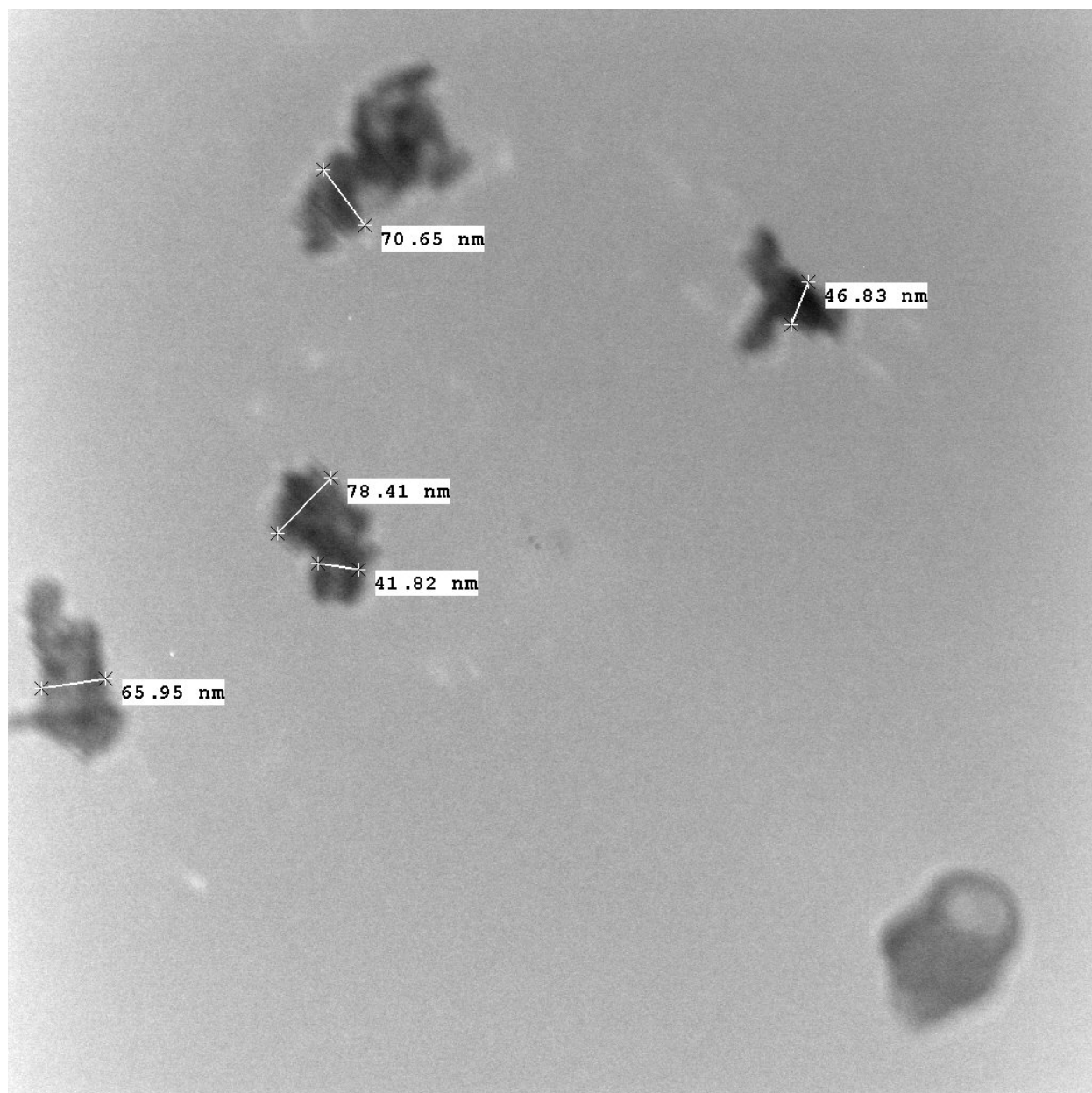
FIGURE 40 - TEM MEASUREMENTS – SAMPLE 6J 006 ZNO.TIF



Sample 7C 002 TiO2.tif
 ZnO
 Print Mag: 160000x @ 7.0 in
 10:28:51 AM 8/10/2012
 Microscopist: ALT

100 nm
 HV=80.0kV
 Direct Mag: 92000x
 AMT Camera System

FIGURE 41 - TEM MEASUREMENTS – SAMPLE 7C 002 TiO2.TIF



Sample 7C 004 TiO2.tif
 ZnO
 Print Mag: 160000x @ 7.0 in
 10:42:00 AM 8/10/2012
 Microscopist: ALT

100 nm
 HV=80.0kV
 Direct Mag: 92000x
 AMT Camera System

FIGURE 42 - TEM MEASUREMENTS – SAMPLE 7C 004 TiO2.TIF